

SUBSTANTIAL DISK–STELLAR MUTUAL INCLINATIONS AND RECURRENT ECLIPSES IN THE YOUNG AND MASSIVE GW ORI TRIPLE SYSTEM

IAN CZEKALA,^{1,*} SEAN M. ANDREWS,² GUILLERMO TORRES,² JOSEPH E. RODRIGUEZ,² ERIC L. N. JENSEN,³
KEIVAN G. STASSUN,^{4,5} DAVID W. LATHAM,² DAVID J. WILNER,² MICHAEL A. GULLY-SANTIAGO,⁶ MICHAEL B. LUND,⁷
RUDOLF B. KUHN,⁸ DANIEL J. STEVENS,⁹ ROBERT J. SIVERD,¹⁰ DAVID JAMES,¹¹ B. SCOTT GAUDI,⁹
KONSTANTIN N. GRANKIN,¹² BENJAMIN J. SHAPPEE,^{13,†} KRZYSZTOF Z. STANEK,^{9,14} THOMAS W.-S. HOLOIEN,^{9,14,15}
CHRISTOPHER S. KOCHANEK,^{9,14} AND JOSE L. PRIETO^{16,17}

¹*Kavli Institute for Particle Astrophysics and Cosmology, Stanford University, 452 Lomita Mall, Stanford, CA 94305, USA*

²*Harvard-Smithsonian Center for Astrophysics, 60 Garden Street, Cambridge, MA 02138, USA*

³*Department of Physics and Astronomy, Swarthmore College, 500 College Avenue, Swarthmore, PA 19081, USA*

⁴*Department of Physics and Astronomy, Vanderbilt University, Nashville, TN 37235, USA*

⁵*Department of Physics, Fisk University, Nashville, TN 37208, USA*

⁶*NASA Ames*

⁷*Department of Physics and Astronomy, Vanderbilt University, 6301 Stevenson Center, Nashville, TN 37235, USA*

⁸*South African Astronomical Observatory, P.O. Box 9, Observatory 7935, South Africa*

⁹*Department of Astronomy, The Ohio State University, Columbus, OH 43210, USA*

¹⁰*Las Cumbres Observatory Global Telescope Network, 6740 Cortona Drive, Suite 102, Santa Barbara, CA 93117, USA*

¹¹*Astronomy Department, University of Washington, Box 351580, Seattle, WA 98195, USA*

¹²*Crimean Astrophysical Observatory, pos. Nauchnyi, Crimea, 298409 Russia*

¹³*Carnegie Observatories, 813 Santa Barbara Street, Pasadena, CA 91101, USA*

¹⁴*Center for Cosmology and Astroparticle Physics, The Ohio State University, 191 W. Woodruff Ave., Columbus, OH 43210, USA*

¹⁵*US Department of Energy Computational Science Graduate Fellow*

¹⁶*Nucleo de Astronomia de la Facultad de Ingeniera, Universidad Diego Portales, Av. Ejercito 441, Santiago, Chile*

¹⁷*Millennium Institute of Astrophysics, Santiago, Chile*

ABSTRACT

We present spatially and spectrally resolved Atacama Large Millimeter/submillimeter Array (ALMA) observations of gas and dust in the large disk orbiting the pre-main sequence hierarchical triple star system GW Ori. We forward-model the ¹³CO and C¹⁸O $J=2-1$ transitions to precisely constrain the total stellar mass to be $5.29 \pm 0.09 M_{\odot}$, and the circumtriple disk inclination to be $i_{\text{disk}} = 137.6 \pm 2.0^\circ$. We use 35 years of optical spectra to derive new radial velocity (RV) solutions and apply spectroscopic disentangling techniques to reveal that the A and B components of GW Ori form a double-lined spectroscopic binary ($P_{\text{in}}=241.50 \pm 0.05$ days) with an outer hierarchical triple ($P_{\text{out}}=4218 \pm 50$ days). Combining the disk and RV measurements with three epochs of archival astrometry yields precise ($\pm 0.3 M_{\odot}$) constraints on the individual stellar masses ($M_A=2.7 M_{\odot}$, $M_B=1.7 M_{\odot}$, $M_C=0.9 M_{\odot}$) and strongly indicates that at least one and possibly both stellar orbits are misaligned with the circumtriple disk by as much as 45° . We also compile a 30-year *V*-band light curve, which reveals several new ~ 30 day eclipse events 0.1 - 0.7 mag in depth. We find a significant 0.2 mag sinusoidal oscillation of the *V*-band flux clearly phased with the outer orbital period, suggesting that the A-B pair is screened by variable degrees of obscuration from material in the inner disk as the outer orbit approaches apoastron. Lastly, we conclude that our measurements of stellar masses and photospheric properties are consistent with the predictions of leading pre-main sequence evolutionary models, and indicate that the GW Ori system is 1.1 ± 0.3 Myr old.

Corresponding author: Ian Czekala
iczekala@stanford.edu

Keywords: protoplanetary disks – stars: fundamental parameters – stars: pre-main sequence – stars: individual (GW Ori)

1. INTRODUCTION

Pre-main sequence stars in multiple systems—for which it is possible to precisely measure their fundamental stellar properties through dynamical means—serve as touchstones for understanding the final stages of stellar formation and the conditions under which planetary systems are assembled. While recent decades have seen steady progress in understanding binary formation in general, lingering uncertainties still remain about the characteristics of young close-in spectroscopic binaries and higher order systems (Duchêne & Kraus 2013). GW Ori, a member of the λ Orionis OB star forming complex (Dolan 2000; Dolan & Mathieu 2001, 2002), was one of the first T Tauri stars to be revealed as a spectroscopic binary, with a composite G spectral type and an orbital period of 240 days (Mathieu et al. 1991). Long term radial velocity monitoring hinted at the presence of a third body in the system with a period of \sim 10 years and was subsequently confirmed by infrared interferometry (Berger et al. 2011). The most recent and precise measurements of the distance to Orion Nebula Complex is a VLBA parallax measurement of 388 ± 5 pc (Kounkel et al. 2017), which we adopt as the distance to GW Ori.

A reservoir of circumstellar material orbiting GW Ori was inferred from near and far-infrared emission in excess of the stellar photosphere (Mathieu et al. 1991), and was subsequently confirmed by a strong single-dish detection of the dust continuum at sub-millimeter wavelengths, suggesting the presence of a massive circumstellar disk ($M_{\text{disk}} \gtrsim 0.1 M_{\odot}$; Mathieu et al. 1995). This detection provided a natural explanation for the quasi-periodic photometric dimminings of GW Ori, which were observed to occur with \sim 30 day durations and were suspected to be due from material in a circumstellar disk around the secondary occulting the primary star at edge-on inclinations (requiring orbital inclinations of $i \approx 90^\circ$; Shevchenko et al. 1992, 1998). Fang et al. (2017) spatially resolved the disk with Submillimeter Array (SMA) observations of the dust continuum and CO isotopologues, and revealed it to be massive ($M_{\text{disk}} = 0.12 M_{\odot}$) and large, with the CO gas significantly more extended ($r_{\text{gas}} \sim 1300$ au) than the dust ($r_{\text{dust}} \sim 400$ au), and

clearly encircling all three stars. However, they found the circumtriple disk to be at an *intermediate* inclination to the line of sight ($i_{\text{disk}} \approx 35^\circ$), challenging the assumption that the GW Ori system is viewed with an edge-on geometry and instead suggesting that more complex dynamics are at play in the innermost radii of the system. Indeed, this adds to the collection of other indirect evidence pointing to a complicated geometry in the inner disk: a spectral energy distribution (SEDs) whose mid-infrared fluxes are variable on the timescale of years (Fang et al. 2014), and mid-infrared spectroscopic detections of CO fundamental emission with line profiles that have both a narrow and broad component, requiring a complicated emission region and temperature structure in the inner disk (Najita et al. 2003).

Beyond resolving outstanding questions about its architecture, given its large nominal primary mass but late composite spectral type ($M_A = 3.9 M_{\odot}$, SpT = G8; Fang et al. 2014, 2017), the GW Ori system presents an excellent opportunity to obtain a precise dynamical mass measurement of a high mass star at a very young age. Precise dynamical masses, especially on the pre-Main Sequence, are crucial to calibrating the photospheric predictions (e.g., T_{eff} , L) of stellar evolutionary models, and the region of the Hertzsprung-Russell diagram (HRD) occupied by GW Ori A is particularly sparsely populated with benchmark systems. GW Ori presents an excellent target for benchmarking because three independent dynamical mass techniques can be brought to bear on it simultaneously: radial velocity monitoring, which constrains the mass ratios of the stars (Mathieu et al. 1991; Fang et al. 2014); astrometric monitoring, which provides the inclinations of the orbits and when coupled with radial velocity measurements can reveal the individual masses of the stars (Berger et al. 2011); and the disk-based dynamical mass technique (e.g., Rosenfeld et al. 2012; Czekala et al. 2015a, 2016), which directly measures the total stellar mass but unlike the first two techniques does not require long-term monitoring, instead the results can be obtained with a single resolved sub-mm observation—an important consideration given the long orbital periods involved.

In this paper, we report resolved sub-mm observations of the GW Ori system with the ALMA interferometer, which confirm the results of Fang et al. (2017) in finding a large and massive protoplanetary disk. We

* KIPAC Postdoctoral Fellow

† Hubble, Carnegie-Princeton Fellow

forward-model the ALMA observations to precisely infer the total mass of the enclosed stars and the disk inclination. We re-analyze 35 years of optical spectra to reveal GW Ori as a low semi-amplitude spectroscopic binary, and derive updated orbital constraints on GW Ori A, B, and C to conclude that the A-B orbit and possibly the AB - C orbit are strongly misaligned with the circum-triple disk. Adding in three epochs of astrometry from Berger et al. (2011) in a joint fit reinforces these conclusions. We evaluate our mass measurements of the stars in context with their photospheric properties to determine their agreement with leading pre-main sequence models. We also present an updated light curve with a 30-year baseline, which shows several new eclipse events and a photometric oscillation phased with the outer orbital period. We conclude by discussing the structure and orientation of the protoplanetary disk with respect to the putative orbital inclinations of the stellar components and place the quasi-period eclipsing nature of GW Ori in the context of other circum-multiple protoplanetary disks.

2. OBSERVATIONS AND DATA REDUCTION

2.1. Millimeter Interferometry

GW Ori was observed with the ALMA interferometer on 2015 May 14 (program ID 2012.1.00496.S), with 37 of the 12 m main array antennas configured to span baselines of 23–558 m. The double sideband Band 6 receivers were employed in dual polarization mode, and the ALMA correlator was set up to process data in 4 spectral windows (SPWs). Two of these SPWs, centered at 220.426 and 230.450 GHz to observe the nearby ^{13}CO and ^{12}CO $J=2-1$ transitions (at rest frequencies of 220.399 and 230.538 GHz, respectively), covered 234 MHz of bandwidth in 3840 channels (a 61 kHz channel spacing). One other sampled 469 MHz around 219.763 GHz to observe the nearby C^{18}O $J=2-1$ transition (at rest frequency 219.560 GHz) with 3840 channels (a 122 kHz channel spacing). The last SPW sampled the continuum in a 1.875 GHz range around 231.956 GHz using 128 coarse channels (a 15.625 MHz channel spacing).

The observations cycled between GW Ori and the quasar J0510+1800 with a 7 minute cadence. The quasar J0423-0120 and Ganymede were observed as bandpass and flux calibration sources, respectively, at the start of the execution block. The total on-source integration time for GW Ori was 16 minutes. The observing conditions were typical for Band 6 projects, with a precipitable water vapor level around 1.1 mm.

The visibility data were calibrated with standard procedures using the CASA software package (v4.4). The raw, observed visibility phases were adjusted based on

the contemporaneous measurements of water vapor radiometers, flagged when applicable, and then the bandpass shape in (and between) each SPW was calibrated based on the observations of J0423-0120. The absolute amplitude scale was determined based on the observations of Ganymede. The complex gain behavior of the array and atmosphere was corrected based on the repeated observations of J0510+1800. The calibrated visibilities showed a strong continuum signal, suggesting that self-calibration could significantly improve the data quality. An initial model based on a preliminary continuum image was used for two rounds of phase-only self-calibration (on 30 s, then 6 s intervals) and one additional round that included the amplitudes (on a 7 minute scan interval). This self-calibration reduced the RMS noise level in the continuum by a factor of ~ 40 . After applying the self-calibration tables to the entire dataset (channel by channel), we parsed out data products for each individual emission tracer of interest. A set of continuum visibilities was constructed by spectrally averaging the line-free channels in each SPW into ~ 125 MHz increments. The spectral visibilities for the ^{12}CO , ^{13}CO , and C^{18}O lines were continuum-subtracted and regridded into 170 m s $^{-1}$ -wide channels in the LSRK restframe over a ~ 10 km s $^{-1}$ range around the line centers.

These fully reduced visibility sets were then imaged by Fourier inversion assuming a Briggs (robust=0.5) weighting scheme and deconvolution with the standard CLEAN algorithm. Some basic image properties for the synthesized continuum image and spectral line image cubes are listed in Table 1. The continuum and spectral line moment maps are shown together in Figure 1, along with a comparison of the integrated spectra. The channel maps for individual lines are compiled in Figure 2.

The 226 GHz (1.3 mm) continuum map shows a bright (flux density = 202 mJy), compact but marginally re-

Table 1. ALMA Image Properties

	RMS	
	beam dimensions	mJy beam $^{-1}$
226 GHz continuum	0''.88 \times 0''.54, 126°	0.055
^{12}CO $J=2-1$	0''.89 \times 0''.56, 126°	6
^{13}CO $J=2-1$	0''.93 \times 0''.59, 126°	8
C^{18}O $J=2-1$	0''.92 \times 0''.58, 126°	5

NOTE—The RMS noise levels recorded for the spectral line cubes correspond to the values per 170 m s $^{-1}$ channel.

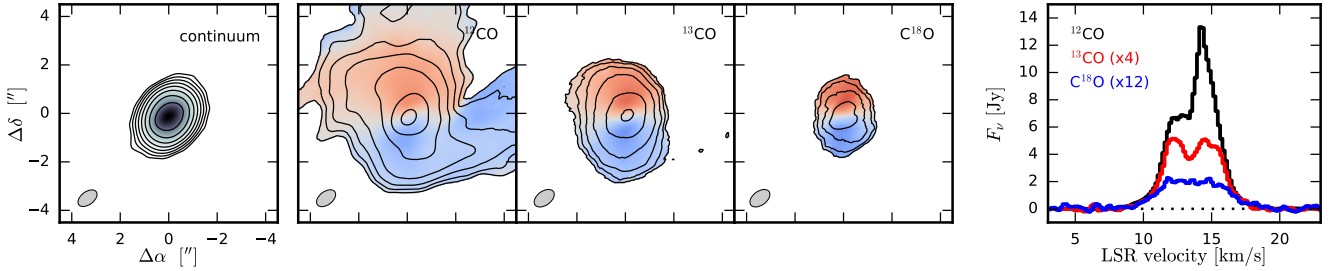


Figure 1. (left) A 226 GHz continuum image. Contours start at $5 \times$ the RMS noise level and increase by factors of 2. The synthesized beam geometry is shown in the lower left corner. (middle, left to right) Maps of the ^{12}CO , ^{13}CO , and C^{18}O velocity-integrated intensities (contours, starting at 10, 3, and 3 \times the RMS noise levels, respectively, and increasing by factors of 2) overlaid on the intensity-weighted projected velocities (color-scale). Note the prominent molecular cloud contamination in the ^{12}CO map (see also Fig. 2). (right) Spatially integrated spectra (inside the same CLEAN mask, and smoothed with an 0.85 km s^{-1} Hanning kernel) for each CO line.

solved (deconvolved Gaussian FWHM $\approx 0''.9$) source centered on the GW Ori stellar system, with a peak intensity of 67 mJy beam^{-1} ($\text{S/N} \approx 1200$). Our integrated flux density measurement is consistent with that of Mathieu et al. (1995, $255 \pm 60 \text{ mJy}$), but marginally discrepant with that of Fang et al. (2017, $320 \pm 64 \text{ mJy}$). A crude estimate of the emission geometry (from a Gaussian fit to the visibilities) suggests an inclination of $35\text{--}40^\circ$ from face-on, with the major axis oriented $\sim 170^\circ$ E of N.

The CO isotopologue channel maps reveal bright (integrated intensities of 41.8 , 5.7 , and 0.8 Jy km s^{-1} for ^{12}CO , ^{13}CO , and C^{18}O , respectively) and extended (FWHM $\sim 2''.5$) emission that is clearly in rotation around the continuum centroid, spanning a projected velocity range of $\pm 5 \text{ km s}^{-1}$ from the line center. The line emission is blueshifted to the south and redshifted to the north, consistent with the orientation estimated from the continuum emission. The peak intensities for each line are ~ 800 , 290 , and 55 mJy beam^{-1} in the brightest channels (peak $\text{S/N} \approx 130$, 35 , and 14) for CO, ^{13}CO , and C^{18}O , respectively. The CO channel maps show some clear evidence for structured contamination from the surrounding molecular cloud, particularly as a streamer to the west at LSRK velocities $\sim 11\text{--}13 \text{ km s}^{-1}$ and some diffuse clumps to the north around $13\text{--}14 \text{ km s}^{-1}$, confirming the “tail”-like structure seen by Fang et al. (2017). These features are much fainter, but still present, in ^{13}CO emission; they are not apparent in the C^{18}O maps.

2.2. Optical Spectroscopy

GW Ori was monitored spectroscopically at the Harvard-Smithsonian Center for Astrophysics for more than 35 years, beginning in 1981 November. A total of 203 usable spectra were gathered through 2009 April using three nearly identical echelle spectrographs (Digital Speedometers, DS; now decommissioned) with a

resolving power of $R \approx 35,000$ mounted on three different telescopes: the 1.5m Tillinghast reflector at the Fred L. Whipple Observatory (Mount Hopkins, AZ), the 4.5m-equivalent Multiple Mirror Telescope (also on Mount Hopkins) before conversion to a monolithic mirror, and occasionally on the 1.5m Wyeth reflector at the Oak Ridge Observatory (in the town of Harvard, MA). Each instrument was equipped with an intensified photon-counting Reticon detector limiting the output to a single echelle order 45 \AA wide, which was centered on the region of the Mg I b triplet at 5187 \AA (see Latham 1992). The signal-to-noise ratios of these observations range from 14 to 59 per resolution element of 8.5 km s^{-1} , with a median of 41. Wavelength calibrations were based on exposures of a Thorium-Argon lamp taken before and after each science exposure. Reductions were performed with a dedicated pipeline, and the zero-point of the velocities was monitored regularly by means of exposures of the evening and morning twilight sky. The original analysis of Mathieu et al. (1991) used a subset of 45 of these spectra. A further 79 usable spectra of GW Ori were collected with the Tillinghast Reflector Echelle Spectrograph (TRES; Fűrész 2008), a bench-mounted, fiber-fed echelle instrument attached to the 1.5m Tillinghast reflector and providing a resolving power of $R \approx 44,000$, delivering 51 orders covering the wavelength interval $3900\text{--}9100 \text{ \AA}$. These observations were made between 2010 November and 2017 April. Signal-to-noise ratios at 5200 \AA range from 28 to 195 per resolution element of 6.8 km s^{-1} , with a median of 74. Wavelength calibration was carried out as above, and reductions were performed as described by Buchhave et al. (2010). Radial-velocity standard stars were observed each night to monitor the zero point and place it on the same system as the DS observations to within $\sim 0.1 \text{ km s}^{-1}$.

All of our spectra appeared initially to be single-lined, with broad features indicative of significant ro-

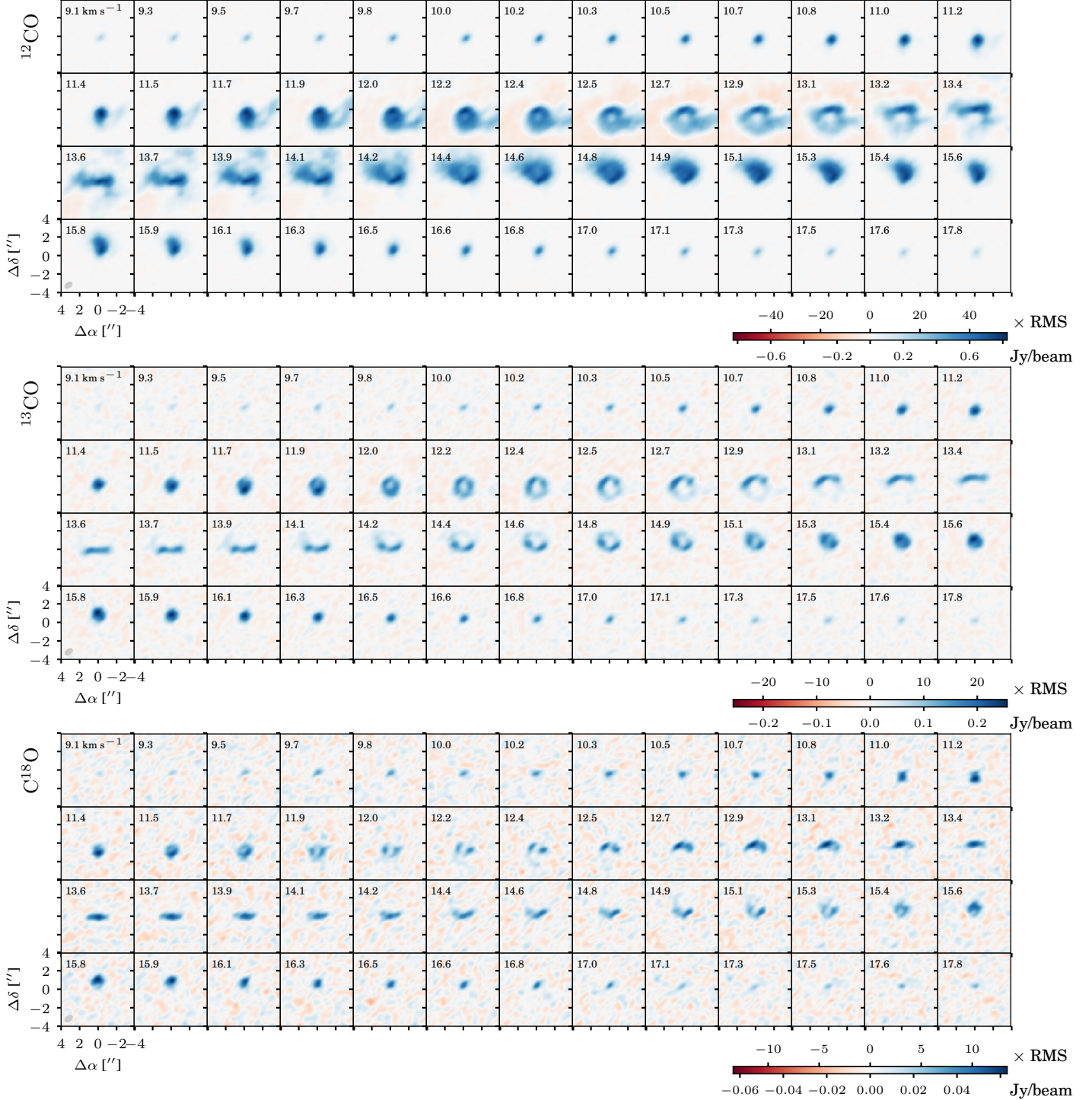


Figure 2. Channel maps of the ^{12}CO , ^{13}CO , and C^{18}O (*from top to bottom*) line emission from the GW Ori disk. Each channel represents the emission in a 170 m s^{-1} -wide velocity bin. LSRK velocities are indicated in the upper left, and synthesized beam sizes in the lower left, or each panel. Scale bars are provided at the bottom right of each set of channel maps.

tation. Preliminary radial-velocity measurements were therefore made with standard one-dimensional cross-correlation techniques, as in the analysis of Mathieu et al. (1991). However, several pieces of evidence suggested it should be possible to detect the lines of the sec-

ondary in the 240 day binary. In particular, the fairly large flux ratio of $f_B/f_A = 0.57 \pm 0.05$ (weighted average) reported by Berger et al. (2011) in the H -band, when translated to the optical, would still be significant for any reasonable assumption on the temperatures of

the stars, making our non-detection of the secondary somewhat surprising. Furthermore, those same authors proposed that the system is observed nearly face-on, which would lead to strong line blending that could explain our lack of detection despite the sizable brightness of the secondary. Additionally, our efforts to disentangle the spectra described later (§3.4) indicated the primary and secondary are indeed separable. Finally, we learned of a detection by others of double lines in targeted high-resolution near-infrared spectra of GW Ori (L. Prato, private communication).

Based on these indications we re-examined our spectra with TODCOR, a two-dimensional cross-correlation algorithm designed to minimize biases in the radial velocities due to line blending, and succeeded in detecting the secondary. As anticipated, the lines of the two stars are always heavily blended, which causes a strong degeneracy between the adopted rotational line broadening for the templates (see below), the velocity amplitudes, the adopted temperatures, and the flux ratio. To measure radial velocities we adopted synthetic templates for the primary and secondary from the PHOENIX library of Husser et al. (2013), broadened to match the resolution of our spectra. For the TRES observations we restricted our analysis to the 100 Å order centered on the Mg I b triplet, both for consistency with the analysis of the DS spectra, which cover only a 45 Å window centered on this region, and because experience shows that it contains most of the information on the velocities. The one-dimensional cross-correlations needed to construct the 2-D correlation function in TODCOR were computed using the IRAF¹ task XCSAO (Kurtz & Mink 1998). The template parameters were selected based on an analysis of the stronger TRES spectra, as follows. For the primary star we adopted a temperature of $T_{\text{eff}} = 5700$ K proposed by Mathieu et al. (1991), along with $\log g = 3.0$ and solar metallicity, although the latter has minimal effect. The same composition and surface gravity were used for the secondary. The rotational broadening ($v \sin i$) of the primary, the secondary temperature, and the secondary $v \sin i$ were then determined by running extensive grids of 2-D cross-correlations over broad ranges in each parameter in a manner similar to that described by Torres et al. (2002), seeking the best match as measured by the peak cross-correlation coefficient averaged over all exposures. For each combination

¹ IRAF is distributed by the National Optical Astronomy Observatories, which are operated by the Association of Universities for Research in Astronomy, Inc., under cooperative agreement with the National Science Foundation.

of template parameters we also determined the flux ratio that maximizes the correlation.

In this way we determined a best-fit secondary temperature of $T_{\text{eff}} = 4800 \pm 200$ K, and $v \sin i$ values for the primary and secondary of 40 and 45 km s⁻¹, respectively, with estimated uncertainties of 5 km s⁻¹. The measured flux ratio in the Mg I b 5187 Å region is $f_B/f_A = 0.25 \pm 0.05$. While in principle these temperatures and $v \sin i$ values are merely free parameters that provide the best match to the observed spectra, in the following we interpret them also as estimates of the physical properties of the stars. The radial velocities we measured from our DS and TRES spectra with these parameters are reported in Table 2, along with their uncertainties. Typical errors for the primary and secondary are 1.0 and 2.7 km s⁻¹ for TRES, and 2.5 and 8.7 km s⁻¹ for the DS measurements. Despite the use of TODCOR, we reiterate that the severe line blending at all phases of the inner orbit caused by a combination of rotational broadening and small velocity amplitudes makes the radial velocities very susceptible to errors in the template parameters (particularly $v \sin i$) and in the adopted flux ratio, and as a result the orbital elements presented later may suffer from systematic errors not included in the statistical uncertainties. Nevertheless, as a consistency check we used PHOENIX spectra from Husser et al. (2013) for the primary and secondary stellar parameters given above to extrapolate our measured flux ratio at 5187 Å to the near infrared, and obtained an *H*-band value of $f_B/f_A = 0.57 \pm 0.12$. While less precise than the Berger et al. (2011) measurement, the agreement is excellent.

2.3. Time-series Photometry

We have assembled a ∼30 year high cadence lightcurve of GW Ori by drawing from several ongoing photometric surveys as well as archival observations. In this section we present the sources of our photometric data and their reduction.

2.3.1. Maidanak Observatory

Text from Grankin.

2.3.2. KELT

The Kilodegree Extremely Little Telescope (KELT) project uses two telescopes to survey over 70% of the entire sky searching for transiting planets around bright stars (8 < V < 11). The telescopes, located in Sonoita, AZ (KELT-North) and Sutherland, South Africa (KELT-South), have a 42mm Mamiya 645-series wide-angle lens resulting in a 26° × 26° field-of-view (FOV), and a 23'' pixel scale. Both telescopes use a broad *R*-band filter.

Table 2. Heliocentric radial-velocity measurements of GW Ori.

HJD (2,400,000+)	RV_A (km s $^{-1}$)	σ_A (km s $^{-1}$)	RV_B (km s $^{-1}$)	σ_B (km s $^{-1}$)	ϕ_{in}	ϕ_{out}
44919.0042	31.24	5.40	28.50	19.13	0.2925	0.8663
45301.8865	25.10	5.18	25.29	18.35	0.8781	0.9572
45336.7941	23.46	3.36	20.37	11.92	0.0226	0.9655
45708.7038	33.05	5.83	20.37	20.65	0.5628	0.0538
45709.6058	37.70	2.76	25.18	9.77	0.5665	0.0540

NOTE—Observations up to HJD 2,454,926.6573 were obtained with the DS, and the remainder with TRES. Phases in the inner and outer orbits are represented with ϕ_{in} and ϕ_{out} . This table is available in its entirety in machine-readable form.

KELT observes using a paramount ME German equatorial mount with a 180° meridian flip; therefore KELT observes in either a “east” or “west” orientation. The telescope optics are not perfectly axisymmetric, and so the point spread function (PSF) changes from one orientation to the other. Throughout the data reduction process, the east and west observations are treated as though they were acquired from separate telescopes. See Siverd et al. (2012) and Kuhn et al. (2016) for a detailed description of the KELT observing strategy and reduction process. GW Ori was located in KELT-South field 05 ($\alpha = 06\text{hr } 07\text{m } 48.0\text{s}$, $\delta = +3^\circ\ 00' \ 00''$) and was observed 2889 times from UT 2010 February 28 until UT 2015 April 09, with a median error of 0.005 mag.

2.3.3. ASAS

Using two observing location, in Las Campanas, Chile and Haleakala, Maui, the All-Sky Automated Survey (ASAS) project was designed to observe the entire sky to a limiting optical magnitude of 14. The two observatory setups each contained a wide-field Minolta 200/2.8 APO-G telephoto lenses with a 2K×2K Apogee CCD and both observed simultaneously in B - and V -band. The telescope and camera set up correspond to a $8.8^\circ \times 8.8^\circ$ field-of-view. ASAS observed GW Ori in the V -band from UT 2001 March 11 until UT 2009 November 29, obtaining 480 observations with a median per-point error of 0.036 mag.

2.3.4. ASAS-SN

Focused on the discovery and characterization of SuperNovae, the the All-Sky Automated Survey for SuperNovae (ASAS-SN, Shappee et al. (2014)) surveys the entire sky down to $V \sim 17$ mag every ~ 2 days. Hosted by the Las Cumbres Observatory (LCO) at

Mount Haleakala, Hawaii and the Cerro Tololo Inter-American Observatory (CTIO) in Chile, each location hosts four 14-cm Nikon telephoto lenses with a 2k × 2k thinned CCD (Brown et al. 2013). The telescopes have a 4.5×4.5 degree field-of-view and a $7.^{\prime}8$ pixel scale. ASAS-SN obtained 799 observations of GW Ori from UT 2014 December 16 until UT 2017 March 15, with a typical per point error of 0.01 mag.

3. ANALYSIS AND RESULTS

3.1. A Reconstruction of the Disk Velocity Field

We use the spatially and spectrally resolved molecular line emission observed with ALMA to tomographically reconstruct the disk velocity field and make a dynamical measurement of the total stellar mass. We follow the forward modeling procedures described by Czekala et al. (2015a, 2016) using the associated open-source software package *DiskJockey*.²

The basis of the parametric physical model adopted in this approach is a radial surface density profile, $\Sigma(r)$, designed to mimic a simple theoretical description for a viscous accretion disk (Lynden-Bell & Pringle 1974; Hartmann et al. 1998). It decreases like $1/r$ interior to a characteristic radius R_c , and has an exponential taper e^{-r/R_c} at larger radii. The vertical distribution (z -direction) of these densities is controlled by the disk temperatures. To convert the total gas densities to molecule-specific values, we start with baseline abundances that are representative of the cold molecular interstellar medium: $[\text{H}_2/\text{gas}] = 0.8$, $[^{12}\text{CO}/\text{H}] =$

² Available under an MIT license at <https://github.com/iancze/DiskJockey>.

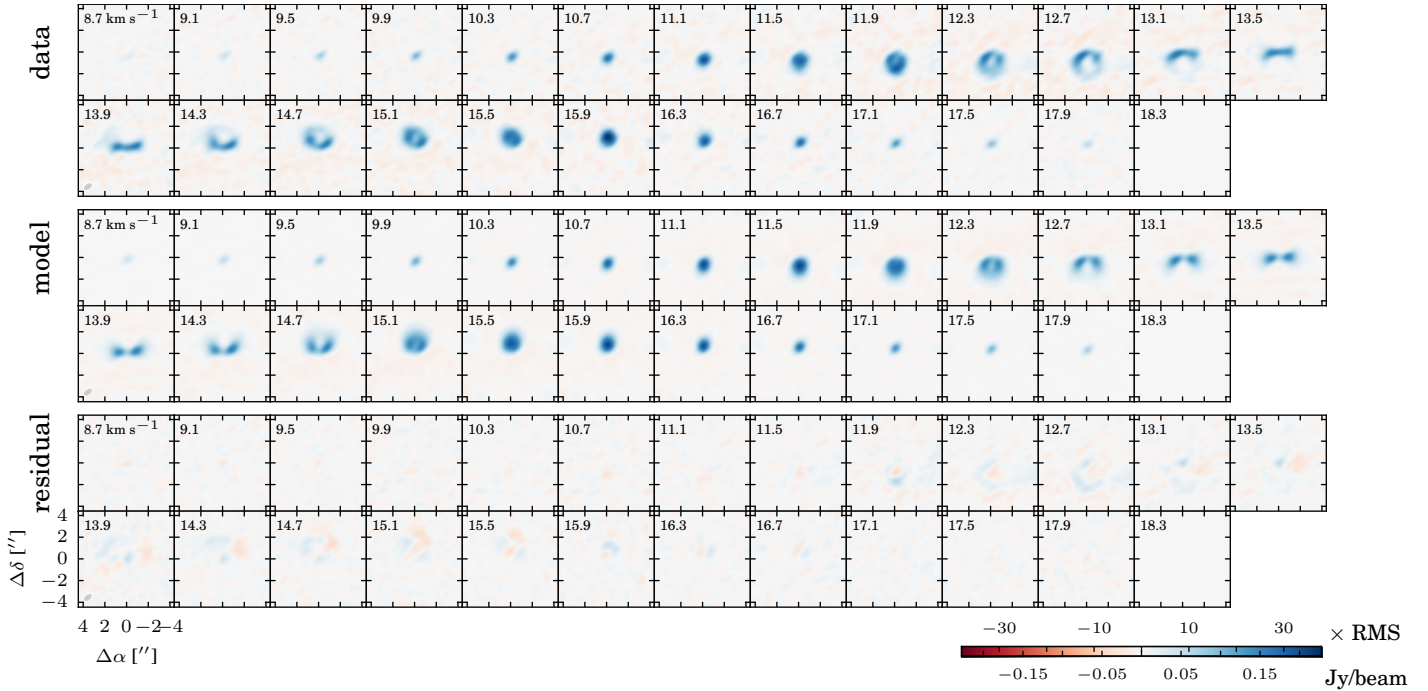


Figure 3. A comparison of the observed channel maps of the ^{13}CO line emission (top) with a best-fit model (middle; constructed from a synthetic visibility set based on the inferred parameters listed in Table 3 and then imaged in the same way as the data) and the associated residuals (bottom; the imaged data–model residual visibilities). The annotation is the same as in Fig. 2.

7.5×10^{-5} , $[^{12}\text{CO}/^{13}\text{CO}] = 69$, and $[^{12}\text{CO}/\text{C}^{18}\text{O}] = 557$ (e.g., Henkel et al. 1994; Prantzos et al. 1996).

The disk kinematics are assumed to be Keplerian and dominated by the total stellar mass M_{tot} , with a velocity field that appropriately accounts for the two-dimensional distribution of the emitting layer (see Rosenfeld et al. 2013). The line-spread function is characterized with a width defined by the quadrature sum of thermal and non-thermal (ξ ; presumably turbulent) contributions. For any physical structure specified by these 6 parameters, $\{\Sigma_c, R_c, T_{10}, q, M_{\text{tot}}, \xi\}$, we solve the molecular rate equations (assuming LTE) and ray-trace the associated emission into a set of high resolution channel maps using the radiative transfer package RADMC-3D (Dullemond 2012). That ray-tracing requires that we specify 3 additional geometric parameters: the disk inclination to the line-of-sight (i_{disk}), the position angle of the disk rotation axis projected on the sky (φ), and the LSRK systemic radial velocity (v_r). Hereafter, we term this parameterization the “standard” model. The model channel maps are then Fourier transformed and sampled at the same spatial frequencies observed by ALMA. The model quality with respect to the observed visibilities is evaluated with a χ^2 likelihood function that incorporates the nominal visibility weights. We assume flat priors on all parameters except for i_{disk} , where we adopt a simple geometric prior (the disk an-

gular momentum vector is distributed uniformly on a sphere, e.g.; Czekala et al. 2016). We adopt a fixed distance to GW Ori of $d = 388$ pc (Kounkel et al. 2017) to make the problem more computationally tractable; we discuss the effects of this assumption in Section 3.3. The posterior distribution of these parameters is explored using Markov Chain Monte Carlo simulations with the affine invariant ensemble sampler proposed by Goodman & Weare (2010), as implemented in the emcee code (Foreman-Mackey et al. 2013) and ported to the Julia programming language, which we include in DiskJockey.

Compared to our previous similar work, the modeling of GW Ori is considerably more computationally intensive. This is primarily a consequence of the large physical size of the disk, which makes the ray-tracing step substantially more time-consuming. The inference for an individual spectral line takes $\sim 10,000$ CPU hours parallelized across 26 cores on the Harvard Odyssey Cluster. Given that restriction and the fact that the ^{12}CO line is clearly contaminated by local cloud material, we restrict our analysis to *independent* inferences of the model parameters based on the ^{13}CO and C^{18}O data only. For computational expediency we only model the data averaged to 25 channels of 0.4 km s^{-1} width. Experiments modeling a subset of the channels at higher

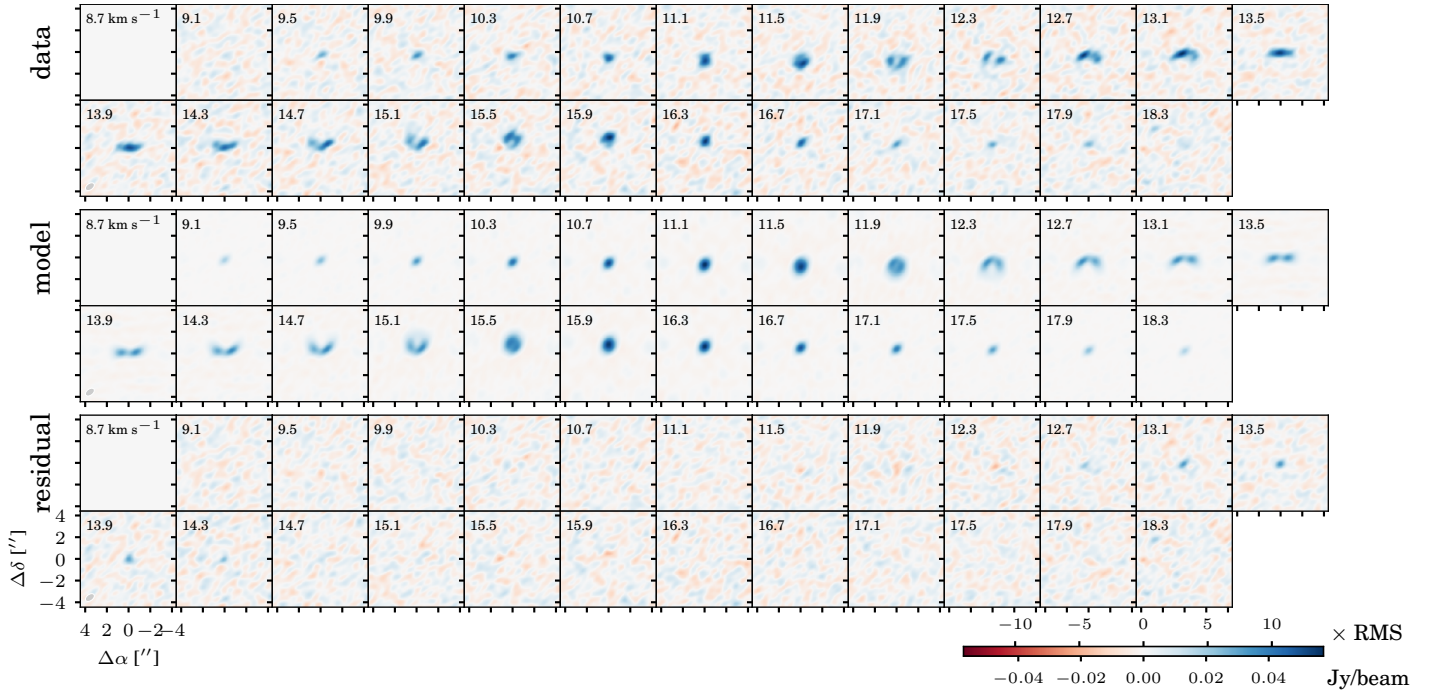


Figure 4. A comparison of the observed channel maps of the C¹⁸O line emission (*top*) with a best-fit model (*middle*; constructed from a synthetic visibility set based on the inferred parameters listed in Table 3 and then imaged in the same way as the data) and the associated residuals (*bottom*; the imaged data–model residual visibilities). The annotation is the same as in Fig. 2.

Table 3. Inferred Disk Model Parameters

Parameter	¹³ CO	C ¹⁸ O
M_* [M_\odot]	5.28 ± 0.06	5.38 ± 0.23
r_c [au]	237 ± 5	151 ± 21
T_{10} [K]	51 ± 2	32 ± 4
q	0.308 ± 0.012	0.378 ± 0.037
$\log_{10} M_{\text{disk}}$	$\log_{10}[M_\odot]$	-1.69 ± 0.02
ξ [km s ⁻¹]	0.59 ± 0.01	0.37 ± 0.03
i_d [deg]	137.7 ± 0.3	135.2 ± 1.4
PA ^a [deg]	90.7 ± 0.1	90.5 ± 0.6
v_r [km s ⁻¹]	13.651 ± 0.003	13.649 ± 0.015
μ_α ["]	-0.004 ± 0.002	-0.028 ± 0.010
μ_δ ["]	-0.044 ± 0.002	-0.051 ± 0.008

^aFor comparison with the stellar orbits, we note that the position angle of the ascending node Ω_{disk} is 90° offset from our PA convention, i.e. $\Omega_{\text{disk}} = \text{PA} + 90^\circ \approx 180.6^\circ$.

NOTE—The 1D marginal posteriors are well-described by a Gaussian, so we report symmetric error bars here.

resolution (e.g., every third channel) did not yield a significantly different result.

The inferred parameter values corresponding to the measurements of each spectral line are summarized together in Table 3. A comparison of the data and the best-fit models (and associated residuals) is presented in the form of channel maps in Figures 3 and 4 for ¹³CO and C¹⁸O, respectively. While overall the models successfully reproduce the observed emission, there are some interesting residuals. Namely, an excess of emission in the center of the disk for the channels between $13.1 - 14.3$ km s⁻¹, seen in both ¹³CO and C¹⁸O. We will return to a discussion of a potential origin in Section 3.5.

Motivated by the presence of the aforementioned residuals, we explored more sophisticated disk models, including a model with a vertical temperature gradient and CO depletion due to freeze-out and photodissociation (after Rosenfeld et al. 2013), as well as a flexible temperature model parameterized to mimic more sophisticated (and computationally expensive) protoplanetary disk models (Kamp & Dullemond 2004; Jonkheid et al. 2004). However, we found that neither of these models resulted in a more satisfactory fit to the data as measured by visual inspection and the Akaike information criterion (AIC). Encouragingly, however, they still yielded similar estimates of M_{tot} as the standard model, which gives us confidence that the disk-based dynamical

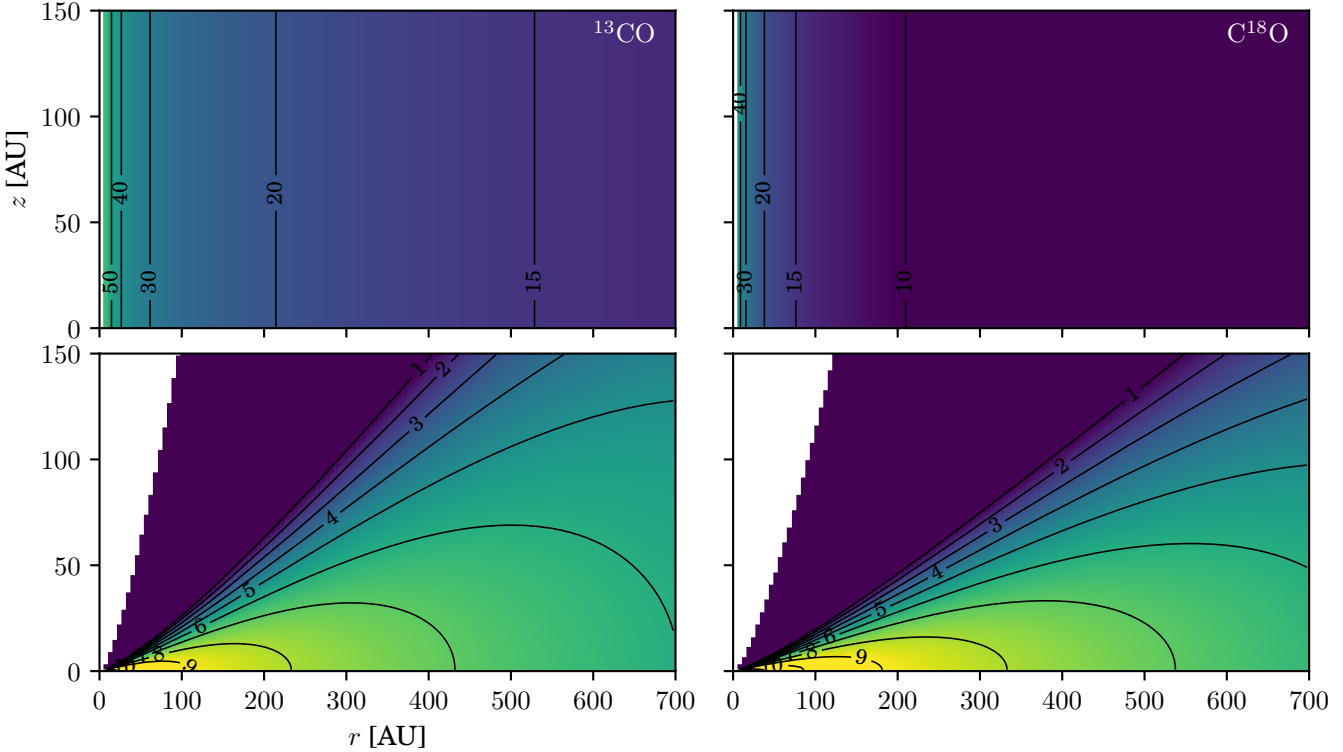


Figure 5. The maximum likelihood 2D temperature (top) and density (bottom) disk structures inferred using the ^{13}CO (left) and C^{18}O (right) transitions. The temperature contours are in units of K. The density plots show the total gas density (ρ_{gas}) and are in units $\log_{10} \text{cm}^{-3}$. The color scales are normalized to the same limits for both transitions.

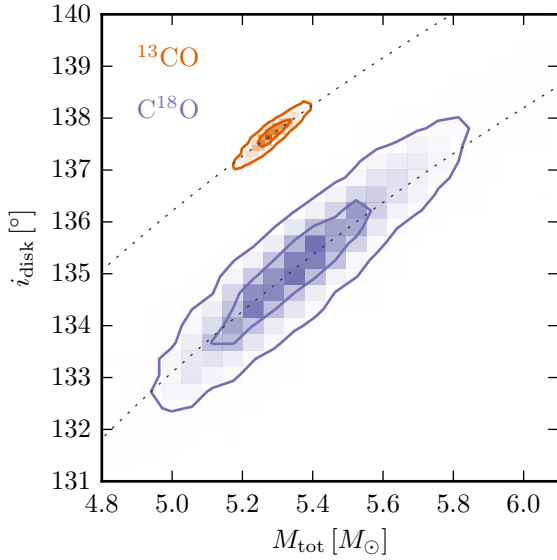


Figure 6. Posterior distributions for the model parameters fit to the ^{13}CO and C^{18}O data independently, showing 1 and 2 σ contours. Dashed lines indicate constant values of $M_{\text{tot}} \sin^2 i_{\text{disk}}$.

mass is moderately robust to choice of parameterization for the temperature and density structures.

Using the standard model, the inferred physical structures inferred from each line are in mild disagreement, as might be expected for this simple parameterization. To illustrate these differences, we plot the 2D temperature and density profiles inferred from each transition in Figure 5. We attribute these differences to the different layers of the disk probed by the ^{13}CO and C^{18}O transitions. In Figure 6, we plot the marginalized posteriors for both transitions in the $\{M_{\star}, i_{\text{disk}}\}$ -plane. Interestingly, the different transitions deliver different inclinations at a statistically significant level ($\Delta i_{\text{disk}} \approx 2.5^\circ$), which we attribute to the previously mentioned model deficiencies and the fact that the ^{13}CO and C^{18}O transitions probe different layers in the disk. This difference is potentially concerning because biases in the measurement of disk inclination have the greatest potential to affect the inference of M_{tot} . With more computational power, it would be worthwhile to explore a joint fit to both transitions, to see if a single disk structure could adequately fit both transitions simultaneously. Nevertheless, both transitions yield consistent constraints on the total stellar mass, which is the most relevant parameter to our stated goals. We believe that the robustness of the dy-

nodynamical mass technique is primarily because the kinematic morphology of the line emission (i.e., the location of the emission in R.A., Dec., and radial velocity space) is not strongly dependent on the exact temperature and density structure of the disk, but is rather a strong function of M_{tot} and i_{disk} , and when the disk is spatially resolved, the dependence on i_{disk} is diminished. We combine the inferred total masses from ^{13}CO and C^{18}O in a weighted mean to find $M_{\text{tot}} = 5.29 \pm 0.06 M_{\odot}$. The uncertainty in the distance to GW Ori (388 ± 5 pc; Kounkel et al. 2017) linearly translates into a mass uncertainty, and so we convolve an additional 1.3% mass uncertainty with this posterior to arrive at $M_{\text{tot}} = 5.29 \pm 0.09 M_{\odot}$, which we adopt as our reported total mass estimate. Because the inferred disk inclinations are mutually inconsistent, we adopt a weighted average for the mean inclination and assume a large systematic uncertainty, resulting in a final estimate of $i_{\text{disk}} = 137.6 \pm 2.0^\circ$. Our CO results are broadly consistent with that determined by Fang et al. (2017), who measure the disk inclination to be $\sim 35 - 40^\circ$.

3.2. An Updated Model of the Stellar Orbits

In this section, we first discuss our orbital fit to the RVs determined in §2.2, and then explore a joint RV + astrometric fit which includes the three epochs of astrometry in Berger et al. (2011). We fit a hierarchical triple orbit and solve for the elements of the inner and outer Keplerian orbits simultaneously, assuming the inner binary acts as a point mass in the outer orbit. To address possible systematic offsets present in the RV dataset, we fit for three offset terms: 1) Δv TRES, applied as a shift to all TRES RVs to account for the offset of the instrumental RV zeropoint 2) Δv_2 Reticon and 3) Δv_2 TRES, offsets which are applied to the secondary RVs to account for possible offset velocities due to template mismatch between the synthetic spectrum used as a cross-correlation template and the true spectrum of the secondary star. The residuals from our initial fit indicated our formal velocity errors are underestimated, and so the uncertainties on each data point are scaled until the final reduced $\chi^2_\nu = 1$ for our final solution.

The period of the inner orbit is consistent with that of Mathieu et al. (1991); Fang et al. (2014); however, due to the SB2 nature of the system, most other orbital parameters have significantly changed. We find a larger semi-amplitude for the primary, $K_A = 8.36 \pm 0.14 \text{ km s}^{-1}$, a mass ratio of $q \equiv M_B/M_A = 0.60 \pm 0.02$, and a statistically significant eccentricity $e_{\text{in}} = 0.13 \pm 0.02$. We find the outer orbit has an orbital period of $P_{\text{out}} = 4218 \pm 60$ days, or 11.5 years, and a statistically significant eccentricity, $e_{\text{out}} = 0.22 \pm 0.09$. We find offset terms

statistically inconsistent with zero: a small but non-negligible offset between the Reticon and TRES zero-points of 0.49 km s^{-1} and larger offsets for the secondary velocities of 8.77 km s^{-1} and 6.41 km s^{-1} , for the Reticon and TRES RVs, respectively. Given the large intrinsic linewidth ($v \sin i \approx 40 \text{ km s}^{-1}$), these large offsets can reasonably be ascribed to template mismatch. All parameters of the RV fit are listed in the first column of Table 4 and the full orbit as a function of time is shown in the second panel of Figure 7. Graphical representations of our observations and the inner and outer orbit models as a function of orbital phase are shown in Figure 8 and Figure 9, respectively.

Although there are only three epochs of published astrometry in Berger et al. (2011), these points may still considerably constrain the parameter space of possible orbits. Therefore, we explore a joint RV-astrometric analysis built upon a model of the “three-dimensional orbit” following Murray & Correia (2010), which adds new model parameters like semi-major axis, orbital inclination, and position angle of the ascending node for both inner and outer orbits. For a likelihood function, we combine the χ^2 RV likelihood and a new χ^2 likelihood for the separation and azimuth measurements of the B and C components relative to the position of A. As with the disk analysis, we also use a geometric prior on the orbital inclinations. For their last measurement epoch (2005), Berger et al. (2011) report an alternate position for the C component, and so we also perform a separate fit as if this were the true location of C. The newly constrained parameters are in the second and third columns of Table 4, and a graphical representation of the orbit is in Figure 10. With the addition of the astrometric dataset, we are able to constrain the individual stellar masses and the inclinations of the orbital planes, which are also listed in Table 4. Depending on whether the original or alternate position for C is used, we find the total stellar mass to be $M_{\text{tot}} = 5.7 \pm 0.7 M_{\odot}$ or $M_{\text{tot}} = 6.1 \pm 0.9 M_{\odot}$, respectively. Both measurements are nicely consistent with the M_{tot} independently measured by the disk-based analysis ($M_{\text{tot}} = 5.29 \pm 0.09 M_{\odot}$).

To measure the degree of misalignment between the orbital planes and the circumtriple disk, we calculate the angle Φ between the angular momentum vectors of each orbit according to Fekel (1981)

$$\cos \Phi = \cos i_1 \cos i_2 + \sin i_1 \sin i_2 \cos(\Omega_1 - \Omega_2). \quad (1)$$

We find that the mutual inclination between the disk and the inner stellar orbit is $\Phi_{\text{in}} = 44 \pm 5^\circ$ and the mutual inclination between the disk and the outer stellar orbit is $\Phi_{\text{out}} = 54 \pm 7^\circ$; these values are similar if one uses the “alternate” C position ($\Phi_{\text{in}} = 45 \pm 5^\circ$,

Table 4. Orbital elements of GW Ori.

Parameter	RV	RV + astrometry	RV + astrometry [†]
Inner orbit			
P [days]	241.49 ± 0.05	241.50 ± 0.05	241.49 ± 0.04
K_A [km s^{-1}]	8.36 ± 0.14	8.34 ± 0.15	8.36 ± 0.15
q	0.60 ± 0.02	0.60 ± 0.02	0.60 ± 0.02
a [au]	1.25 ± 0.05	1.27 ± 0.05
e	0.13 ± 0.02	0.13 ± 0.01	0.13 ± 0.01
i [deg]	157 ± 1	157 ± 1
ω_A [deg]	196 ± 7	197 ± 7	196 ± 6
Ω^b [deg]	263 ± 13	264 ± 13
T_{peri} [HJD–2,400,000]	56681 ± 4	56682 ± 4	56681 ± 4
γ [km s^{-1}]	$+28.31 \pm 0.19$	$+28.33 \pm 0.18$	$+28.29 \pm 0.19$
Δv TRES ^a [km s^{-1}]	0.49 ± 0.24	0.52 ± 0.23	0.47 ± 0.23
Δv_2 Reticon ^a [km s^{-1}]	8.77 ± 0.65	8.75 ± 0.67	8.73 ± 0.66
Δv_2 TRES ^a [km s^{-1}]	6.41 ± 0.37	6.36 ± 0.35	6.39 ± 0.39
M_A [M_\odot]	$2.80^{+0.36}_{-0.31}$	$2.94^{+0.40}_{-0.40}$
M_B [M_\odot]	$1.68^{+0.21}_{-0.18}$	$1.77^{+0.24}_{-0.24}$
Outer orbit			
P [days]	4218 ± 60	4246 ± 66	4203 ± 60
K_{AB} [km s^{-1}]	2.47 ± 0.25	2.38 ± 0.23	2.50 ± 0.24
a [au]	9.19 ± 0.32	9.15 ± 0.35
e	0.22 ± 0.09	0.13 ± 0.07	0.25 ± 0.08
i [deg]	150 ± 7	144 ± 9
ω_{AB} [deg]	307 ± 18	310 ± 21	310 ± 12
Ω^b [deg]	282 ± 9	263 ± 10
T_{peri} [HJD–2,400,000]	53560 ± 565	53911 ± 260	53878 ± 130
M_C [M_\odot]	$1.15^{+0.40}_{-0.23}$	$0.99^{+0.35}_{-0.18}$
Derived properties			
Inner time interval [cycles] ..	53.6
Outer time interval [cycles] ..	3.1
$M_A \sin i$ [M_\odot]	0.30 ± 0.02
$M_B \sin i$ [M_\odot]	0.18 ± 0.01
$M_C \sin i / (M_{\text{tot}}/M_\odot)^{2/3}$ [M_\odot]	0.22 ± 0.02
M_{tot} [M_\odot]	5.7 ± 0.7	6.1 ± 0.9

^aWe include parameters for a potential velocity offset between the primary and secondary radial velocities for each instrument. In principle, this term should be consistent with 0; the non-zero value likely indicates that there is some moderate template mismatch between the secondary stellar spectrum and the synthetic spectrum used as a cross correlation template.

^bWe follow the convention of the visual binary field and define the ascending node as the line of nodes where the secondary component (e.g., star B for the inner orbit, and star C for the outer orbit) crosses the plane of the sky moving *away* from the observer.

[†]Fit using the “alternate” C position for the 2005 epoch of astrometry in Berger et al. (2011).

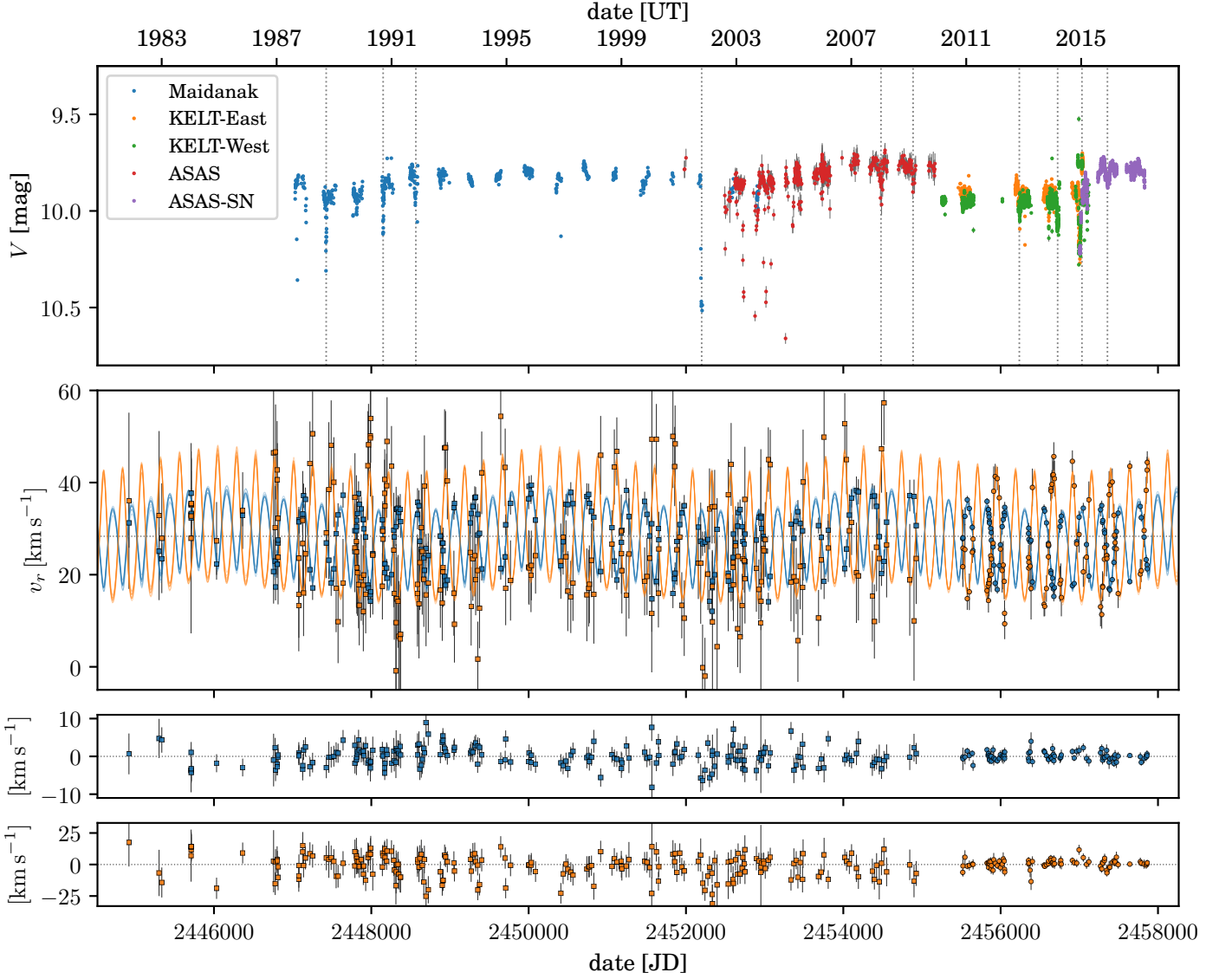


Figure 7. *top:* photometric observations of GW Ori from 1987 until mid 2017. All photometric observations displayed here are in the V -band (ASAS, ASAS-SN, and Maidanak) or a broader filter (KELT) which has been shifted to align with V -band where the time series overlap. *bottom:* primary (blue) and secondary (orange) radial velocities overlaid with several realizations of the most probable orbits, to show uncertainty in the orbit. Reticon velocities are shown with squares, TRES velocities are shown with circles, and the dotted line represents the center-of-mass velocity. Residuals for this orbit are shown in the panels below.

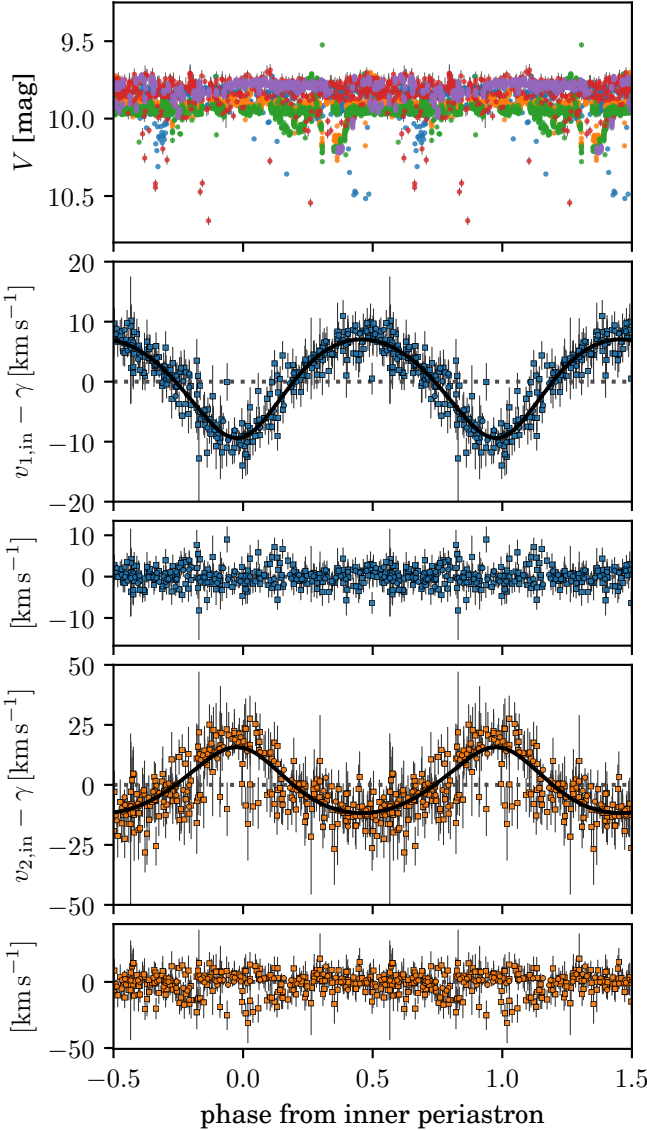


Figure 8. *top:* V -band light curve phased to the inner orbital period. No discernible correlation is detected. *bottom:* RV measurements of GW Ori and best-fit model for the inner orbit, after subtracting the motion due to the outer orbit.

$\Phi_{\text{out}} = 50 \pm 6^\circ$). Such a large misalignment is surprising given the naive expectation that the stellar orbits and disk would be roughly co-planar. Since these results only rest upon three astrometric epochs, however, there is a possibility that the large inferred mutual inclinations may be the result of unaccounted for systematic effects. In the next section, we use only the newly derived RVs and disk-based dynamical mass to formulate a more conservative estimate of the mutual inclinations. We advocate continued astrometric monitoring of the GW Ori system to further improve the three-dimensional orbit

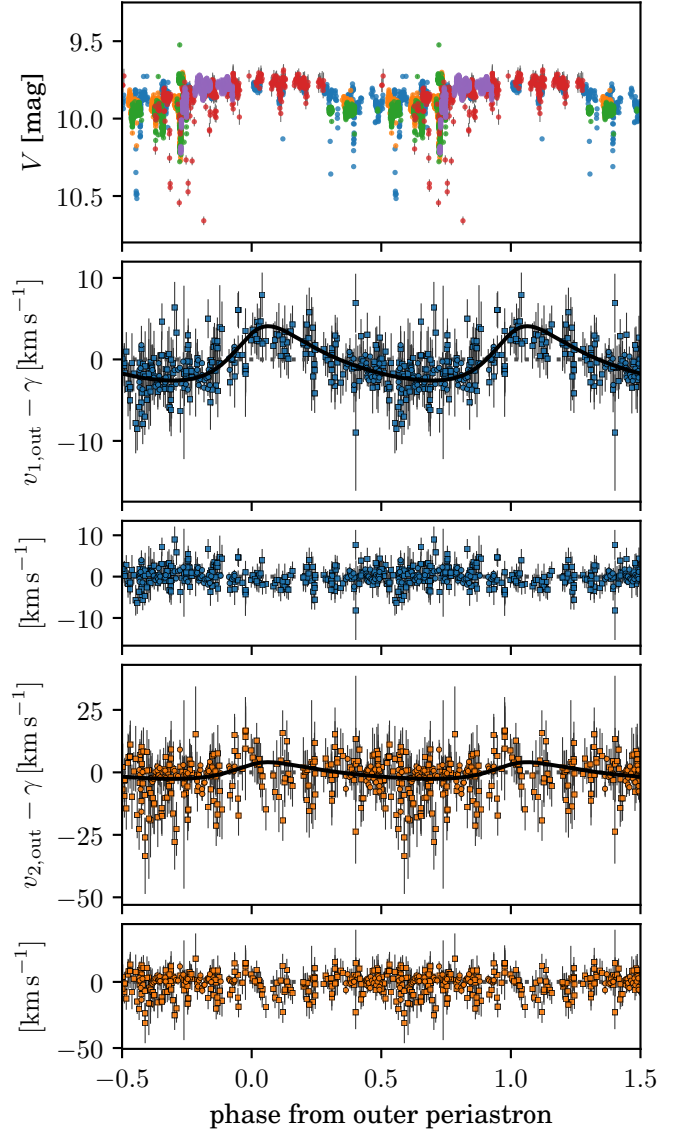


Figure 9. *top:* V -band light curve phased to the outer orbital period, showing that the mean flux level oscillates by 0.2 mag over the course of the outer orbit, and is lowest during apoastron (phase 0.5). *bottom:* RV measurements of GW Ori and best-fit model for the outer orbit, after subtracting the motion due to the inner orbit.

and definitively confirm the inclinations of the stellar orbits.

3.3. Joint Radial Velocity and Disk Constraints on Individual Component Masses

In this section, we combine the double-lined RV constraints with the disk-based constraints on the total stellar mass to form an independent constraint on the individual stellar masses of the GW Ori system without referencing the Berger et al. (2011) astrometry.

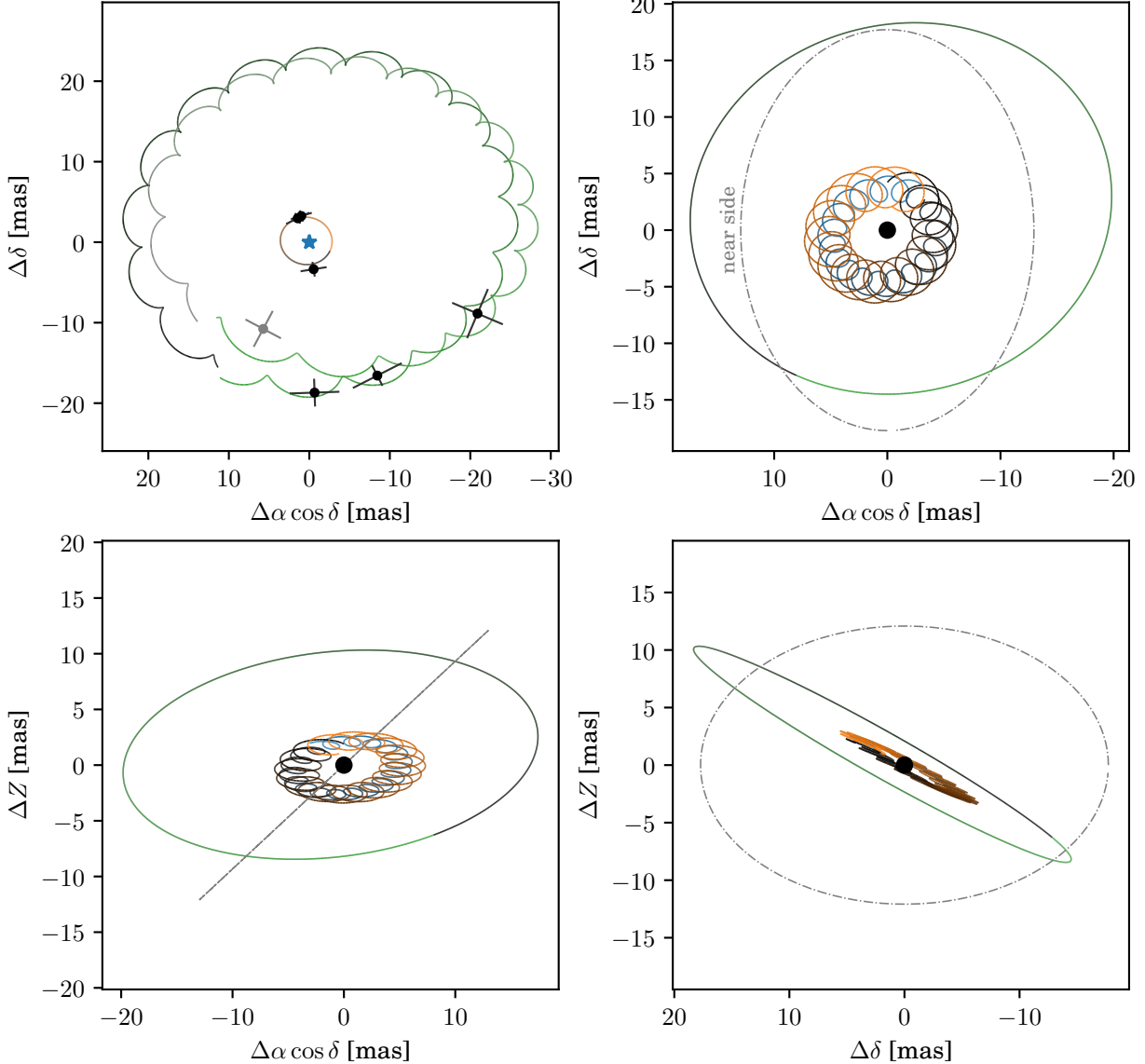


Figure 10. Orbits from the joint RV-astrometric fit shaded according to their phase, where black represents periastron and color hue increases with orbital phase. *top left:* orbits relative to the primary star A, in the plane of the sky, with the three epochs of astrometry from Berger et al. (2011). The light grey data point and outer orbit represent the fit to the ‘‘alternate’’ position for C. The following plots are relative to the center of mass of the system. A fictitious particle at 7 au on a circular orbit coplanar with the circumtriple disk is shown as grey dashed line. *top right:* the sky plane. For future discussion in §3.5, we label the side of the disk nearest to the observer. *bottom left:* looking down the North axis. *bottom right:* looking down the East axis. Positive Z points towards observer.

We construct a joint likelihood function with the following five parameters: M_A , M_B , M_C , i_{in} , and i_{out} . The double-lined radial velocity constraints are sufficiently captured by the summary statistics $M_A \sin^3 i_{\text{in}}$, $M_B \sin^3 i_{\text{in}}$, $M_C \sin i_{\text{out}} / (M_{\text{tot}}/M_{\odot})^{2/3}$ and the covariances between them, which are well represented by

a multivariate Gaussian distribution.³ The disk constraint on the total stellar mass M_{tot} is well-represented by a Gaussian, as well. We enforce flat priors on the stellar masses and geometrical priors on the inclinations. We use the ensemble sampler MCMC (Goodman

³ Note that we do not use additional constraints on q_{in} or other derived parameters, as this would amount to double-counting the RV constraints.

Table 5. Joint constraints on stellar masses and orbital inclinations

Parameter	RV + astrometry	RV + disk
$M_A [M_\odot]$	$2.80^{+0.36}_{-0.31}$	$2.74^{+0.15}_{-0.52}$
$M_B [M_\odot]$	$1.68^{+0.21}_{-0.18}$	$1.65^{+0.10}_{-0.31}$
$M_C [M_\odot]$	$1.15^{+0.40}_{-0.23}$	$0.88^{+0.85}_{-0.19}$
i_{in} [deg]	157^{+1}_{-1}	151^{+1}_{-2}
i_{out} [deg]	150^{+7}_{-7}	130^{+28}_{-27}

NOTE—The RV + astrometry values are replicated from Table 4 for comparison purposes. We note that we are not able to infer the absolute inclination of the stellar orbits directly from the radial velocity data, so there is in fact an alternate solution for the RV + disk results that yields $i_{\text{alt}} = 180^\circ - i$. This solution would be inconsistent with the astrometric motion, however, so we opt to only report the solutions with $i \geq 90^\circ$.

& Weare 2010; Foreman-Mackey et al. 2013) with 20 walkers to explore the posterior for 50,000 iterations, burn 25,000 iterations, and assess convergence by ensuring the Gelman-Rubin statistic (Gelman et al. 2014) is $\hat{R} < 1.1$ for all parameters.

This analysis produces consistent but less precise constraints on the stellar masses as the joint RV + astrometric fits (see Table 5). Like the RV + astrometric analysis, the disk + RV analysis also indicates that the inner stellar orbit must be significantly misaligned with the disk, although the true misalignment is unknown: the difference between i_{in} and i_{disk} only provides a lower limit on the mutual inclination because the true mutual inclination must consider the position angles of the orbits as well. To highlight these findings, we overplot our newly derived constraints on the disk inclination and the stellar orbits in Figure 11. At the lowest inclinations (nearest to edge-on, $i = 90^\circ$) are the measurements for the disk in ^{13}CO and C^{18}O . This is commensurate with the disk inclination measurements from Fang et al. (2017), and so we consider these results to be robust. Interestingly, the constraints on i_{in} differ between the RV + astrometry and the RV + disk results at a significant level. We speculate that this difference might be due to unknown systematics in the astrometry or RV datasets, or potentially an error in our assumption of the distance to GW Ori. While the astrometry + RV analysis does not require a distance to the source, the disk-based analysis does require a distance in order to break the M_{tot}/d degeneracy. Although the exact degree of mutual inclination between the inner orbit and the disk is unknown, we conclude that it is likely that it is at least 10° and potentially as high as 45° . The RV + disk constraints on the outer orbit are less precise, but also suggest that the planes are at least somewhat misaligned.

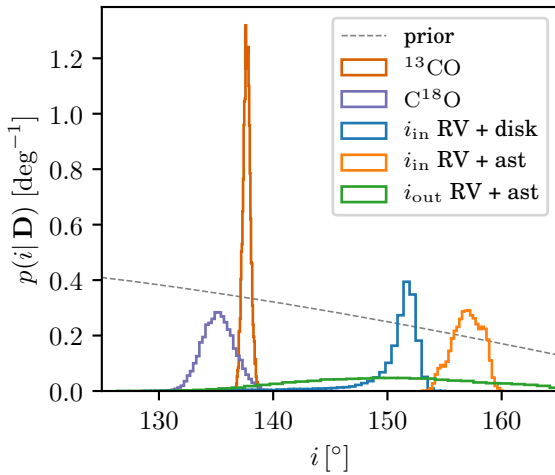


Figure 11. The inclination posteriors on the disk inclination, inner stellar orbit, and outer stellar orbit, as determined from various joint fits. Because i_{out} is essentially unconstrained by the RV + disk analysis, it is not plotted for aesthetic reasons. The geometric prior on inclination (uniform orientation of orbits in 3D space) is shown as a thin grey dotted line.

3.4. Disentangling the GW Ori Double-lined Spectroscopic Binary

As we noted in §2.2, at optical wavelengths GW Ori clearly appears to be a *single-lined* spectroscopic system, despite full coverage of the 240 day inner period at moderate to high S/N (Mathieu et al. 1991; Fang et al. 2014). In this context, the Berger et al. (2011) H-band detections of the secondary and tertiary stars at favorable flux ratios ($f_B/f_A = 0.57 \pm 0.05$ and $f_C/f_A = 0.23 \pm 0.01$) were rather puzzling, since such a bright secondary companion should have detectable optical signatures. We originally embarked on a search for these signatures using the then-under-development PSOAP spectroscopic disentangling package (Czekala et al. 2017), with a strong assumption that these spectral signatures must be at or near the detection limit (e.g., $q_{\text{in}} \lesssim 0.2$), since they had not been seen in previous analyses. Our preliminary results hinted at the detection of a secondary spectrum, but with mass ratios much larger than what we had expected ($q_{\text{in}} > 0.5$). Because the algorithm was still under development, we discounted these initial

results as spurious and possibly the result of contamination by stellar variability. To our excitement, however, shortly thereafter we learned that GW Ori had been revealed as a *double-lined* spectroscopic binary using targeted high resolution infrared spectroscopy ($q_{\text{in}} \sim 0.65$, L. Prato, private communication, March 2017). Using this knowledge, we renewed our efforts to search for the secondary signature using PSOAP and targeted TODCOR analysis.

The PSOAP spectroscopic disentangling technique works as an inference framework. Given a time-series of high resolution spectroscopic observations covering the orbital phase of the binary or triple star, it simultaneously infers the intrinsic spectrum of each star along with the stellar orbit. PSOAP uses Gaussian processes to model the unknown stellar spectra, providing a robust probabilistic framework by which the spectra and orbits can be inferred in a purely data-driven manner. Once disentangled, these spectra can be used to infer fundamental stellar properties by traditional analysis techniques. For more information on the mathematical details of PSOAP please consult Czekala et al. (2017). At present, one limitation of the PSOAP framework (and Gaussian processes in general, to some extent) is the heavy computational requirement for performing the matrix calculations. This generally limits us to considering less than 20 epochs of high resolution spectra at a time, which consequentially limits the complexity of the orbital model that we can use. Although it was straightforward to extend the framework to utilize a hierarchical triple orbital model and three Gaussian process components, we found that we were unable to employ enough spectroscopic epochs to sufficiently constrain the more complex orbital model. Therefore, we experimented using different subsets of the highest S/N data to test our sensitivity to presence of secondary and tertiary spectral signatures. In particular, we found the most success when we used 40 Å of spectra containing many deep absorption lines between 5160 and 5200 Å broken up into 5 Å chunks. In all of these tests, we clearly detected the features of the secondary but found no solid evidence for spectroscopic signatures of the tertiary. We have identified possible avenues of development to expand the number of spectroscopic epochs under consideration, but exploring these options will require development and testing beyond the scope of this paper.

While PSOAP unfortunately has a limited ability to constrain the orbital parameters of GW Ori, it can still provide disentangled spectra of the primary and secondary stars. We use the 16 highest S/N spectra and assume the best fit radial velocity orbit specified in §3.2

to disentangle a wide wavelength range of data covering 5060 - 5290 Å. The disentangled spectra are shown in Figure 12, overlaid with two representative Husser et al. (2013) models using the same stellar parameters as determined by the cross-correlation analysis described in §2.2. In general, an inherent limitation of disentangling techniques is that they are unable to provide any information on the flux ratios of the components: they are only able to provide the relative amplitudes of the spectral variations. Essentially, there emerges a degeneracy between a bright companion star with shallow spectral lines and a faint companion star with deep spectral lines. Therefore, in order to re-normalize⁴ the disentangled spectra to compare with synthetic models, we must assume a flux ratio between the two stars. In light of this, the process of inferring stellar parameters becomes rather difficult, especially since both GW Ori A and GW Ori B may suffer from veiling and both the re-normalization and veiling affect the “contrast” level of the spectra. Over this narrow wavelength range, T_{eff} mainly changes the depth of the lines, while $\log g$ and $v \sin i$ mainly change the shape and depth of the lines. Due to these degeneracies, we are encouraged that the disentangled look like the spectra used to derive the radial velocity solutions, but note that in reality, the stellar parameters could plausibly range by $\Delta T_{\text{eff}} \sim 500$ K, $\Delta \log g \sim 0.5$ dex, and $\Delta v \sin i \sim 10$ km s⁻¹ in a correlated manner for each star, especially given uncertainties about the flux ratio and accretion veiling. Further analysis using a broader wavelength range may help alleviate some of these degeneracies.

3.5. Periodic Dimming and Eclipses

Using the longer baseline of our combined lightcurve, we identify several new eclipse events, bringing the total number of known events to 13. The 10 events covered by our lightcurve are listed in Table 6, marked in Figure 7, and shown zoomed in Figure 13. Given the sometimes considerable noise in our lightcurve, we have only identified eclipse events that show multiple consecutive photometric points deviating significantly from the running average, since a large dip in only one epoch of photometry is likely the result of a spurious observation. There are also regular seasonal gaps in the lightcurve, making it likely that many other eclipse events were missed due to lack of coverage. The eclipse events are broadly similar in depth and duration to the events identified

⁴ Note that this is *not* continuum normalization in the traditional sense (e.g. dividing by a spline fit to the stellar continuum), but simply a constant scaling by a ratio defined in Czekala et al. (2017, Eqn. 32) which preserves broad-scale shapes intrinsic to the spectra.

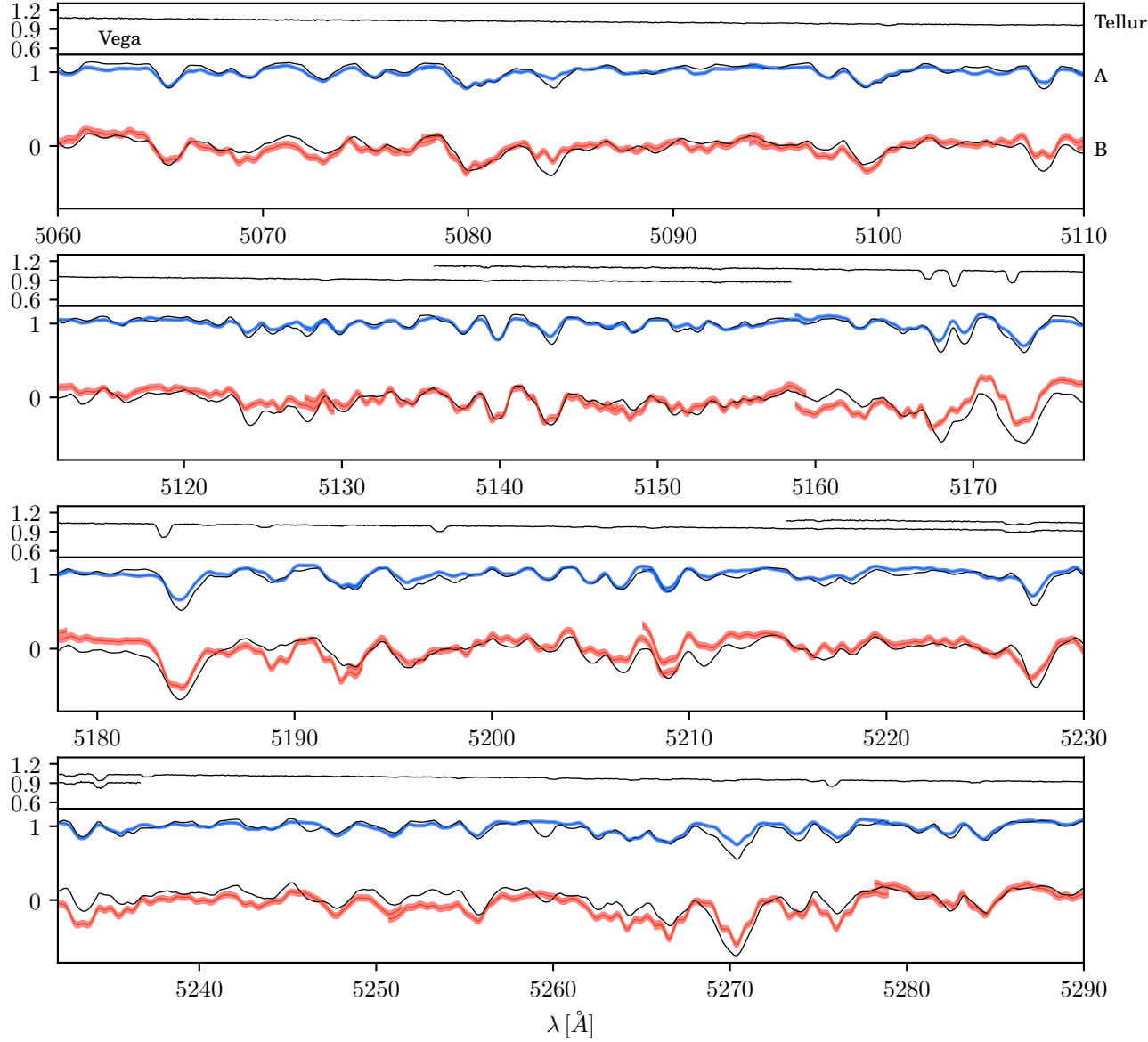


Figure 12. The disentangled spectra of GW Ori A and GW Ori B in blue and red, respectively. The top bar shows a spectrum of Vega, to demonstrate that this wavelength band is free from any telluric line contamination. The disentangled spectra have been inversely scaled by an assumed flux ratio to bring their continuum level to 1 to facilitate better comparison to the synthetic models. Disentangled spectra at the edges of echelle orders may appear jagged (e.g. $\sim 5160 \text{ \AA}$). In this figure, we have assumed the same flux ratio and stellar parameters as found by the cross-correlation analysis described in §2.2: $f_B/f_A = 0.25$, the primary is $T_{\text{eff}} = 5700 \text{ K}$, $\log g = 3.0 \text{ dex}$, $v \sin i = 40 \text{ km s}^{-1}$, the secondary is $T_{\text{eff}} = 4800 \text{ K}$, $\log g = 3.0 \text{ dex}$, $v \sin i = 45 \text{ km s}^{-1}$.

in Shevchenko et al. (1992, 1998), ranging from 0.1 to 0.7 mag and lasting between 10 to 50 days. While there are several sequential eclipse events that occur near the inner period of 241 days (e.g., the first two eclipses in 1988 and 1990 noted by Shevchenko et al. (1992)), our longer baseline reveals that the eclipses are not strictly periodic. When the full lightcurve is phased to the inner period (Figure 8), it becomes clear that there are a multitude of inner phases at which the eclipse events occur. We do observe one potential brightening event,

shown in the lower left panel in Figure 13. Brightenings are not seen for other eclipse events, so this case may be a unique artifact present in the KELT data, especially since the ASAS-SN data, which covers from egress onward, does not show the same behavior. If this event is indeed real, then it would indicate increased accretion or flare luminosity during the eclipse itself. If this timing were not simply a coincidence, then this would indicate a direct link between the eclipses and accretion onto the stellar surface.

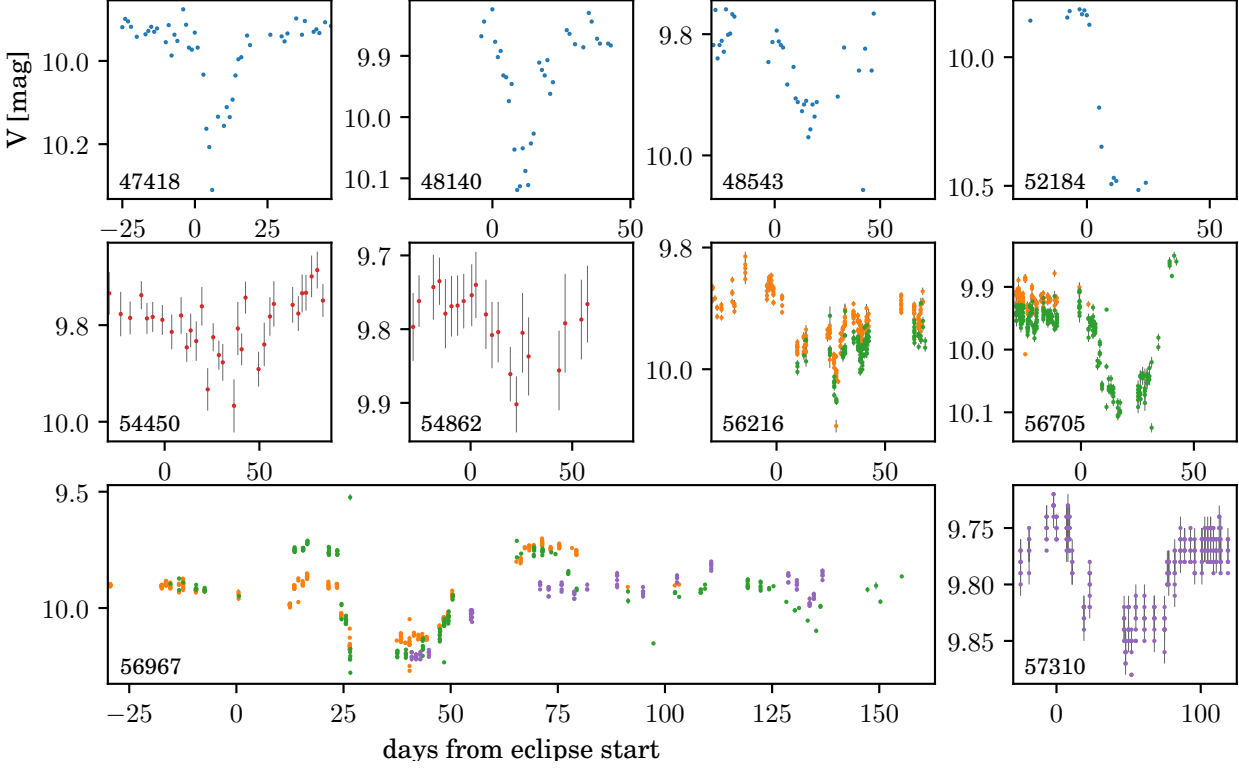


Figure 13. A gallery of the eclipse events noted in Table 6, labeled relative to the start of the eclipse. The legend is the same as in the top panel of Figure 7. Note that the y-axis scale is significantly different from panel to panel, with some eclipses as deep as 0.7 mag and others less than 0.1 mag. The first two events are the same events identified by Shevchenko et al. (1992).

Table 6. V-band Photometric Eclipse Catalog

Start	End	Duration	Depth	Telescope
JD	JD	days	mmag	
2447418	2447435	17	400	Maidanak
2448140	2448161	21	350	Maidanak
2448543	2448589	46	150	Maidanak
2452184	≥ 2452215	≥ 31	700	Maidanak
2454450	2454508	58	100	ASAS
2454862	2454912	50	150	ASAS
2456216	2456259	43	110	KELT
2456705	2456744	39	200	KELT
2456967	2457100	30-130	250	KELT/ASAS-SN
2457310	2457405	95	100	ASAS-SN

Eclipses notwithstanding, the most striking mode of variability that emerges with the long baseline of our lightcurve is a 0.20 mag sinusoidal oscillation of the mean non-eclipsed flux, clearly phased with the outer orbital period of 4218 days (Figure 9). We must be care-

ful when evaluating this mode of variability, however, since it stretches across photometry acquired from several different instruments. Moreover, the KELT dataset was not taken in V-band but rather shifted to match the overlapping ASAS-SN observations, which means that it has limited ability to constrain this longer mode due to zeropoint uncertainty. With these caveats in mind, given that clear rising and falling trends are seen within each data set and that no vertical shifts have been applied to any other dataset, this mode is likely real. A final supporting piece of evidence is the earlier photoelectric observations of Shevchenko et al. (1998), which stretch back to JD 2,445,000 and clearly phase up with the expected sinusoidal variation. Beyond this long term variability, it appears as if the deep eclipses preferentially occur between phases 0.4 - 0.8 from periastron. However, when consulting the earlier photometry in Shevchenko et al. (1998), we find at least two additional eclipses that fall closer to 0.0 phase, suggesting that the apparent clustering of deep eclipses is an effect of the seasonal sampling in our dataset.

The long period sinusoidal variability reaches minimum flux levels near apoastron (phase 0.5) of the outer orbit. Since the light from the A-B binary dominates the total optical flux from the system, it is one or both

of these stars that are either being partially occulted by opaque material (e.g., the sharp edge of a dense dust ring) or more fully occulted by partially opaque material (e.g., diffuse dust). When the A-B system is at apoastron it is closest to the inner edge of the disk (see Figure 10, top right panel), which has presumably been somewhat cleared due to the dynamical influence of the stellar components. Due to the fact that the disk is more edge-on than the stellar orbits, apoastron also happens to correspond to the time when the A-B pair comes closest to being screened by the inner edge of the near side of the disk. From dynamical arguments, we expect the inner edge of the disk to be truncated out to 2-3 times the semi-major axis of the tertiary, which corresponds to $\sim 20\text{-}30$ au in radius. Even with the foreshortening due the relative inclinations, the inner edge of the disk would be at too large of a projected distance to occult the A-B pair at apoastron, unless the inner edge of the disk was very puffed up. Given the gradual dimming, it may be more likely that the A-B pair is screened by tenuous material residing inside this truncation radius, such as the micron-sized dust within the gap hinted at by the $10\mu\text{m}$ silicate emission feature in the SED (Fang et al. 2014). By modeling the spectral energy distribution of GW Ori, Fang et al. (2014) determined that there is a variable reservoir of small grains in the center of the disk, possibly cleared and replenished due to the actions of the tertiary.

We also see excess ^{13}CO and C^{18}O emission above our standard disk model at locations consistent with this near edge of the disk, but at or near the systemic velocity of the system ($13.1\text{ - }14.3\text{ km s}^{-1}$). This excess could simply be an artifact from using an insufficiently complex disk model, but if it is real, it may very well be the source of the eclipses or long term dimming, or both. An outstanding question is what does the disk look like on the scales of the inner orbit? Our ALMA observations do not have sufficient angular resolution to probe the disk at the physical scales corresponding to the orbit of the triple, and beyond the knowledge that the solids are constrained to smaller radii ($r_{\text{dust}} \sim 600$ au) than the gas ($r_{\text{CO}} \sim 1300$ au), the distribution of solids within the GW Ori disk is not especially well known. At its longest baselines, ALMA would have the spatial resolution (0.02 arcsec) to probe the disk on 8 au scales, more than sufficient to resolve a hole on the scale of the outer orbit (18 au or larger in diameter).

Given that the ~ 30 day eclipse events do not significantly sync with the outer orbital period, it is not immediately clear whether they share the same physical origin as the long term brightness variations. The quasi-periodic nature of these eclipses, whereby a deep eclipse

occurs and then subsequent shallower eclipses occur during the next orbit, led Shevchenko et al. (1998) to attribute these eclipses to an occultation by the overflowing Roche lobe of the secondary star. As the material accreted onto the secondary star, the size of the occulter diminished, and the eclipses got shallower. We now know from dynamical constraints that an edge-on A-B orbit ($i_{\text{in}} \approx 90$ deg) is ruled out, and so we must consider other mechanisms. While do not see a series of eclipses with such striking regularity as those observed by Shevchenko et al. (1998), it does appear as though consecutive eclipses may be correlated with the 241 day inner period.

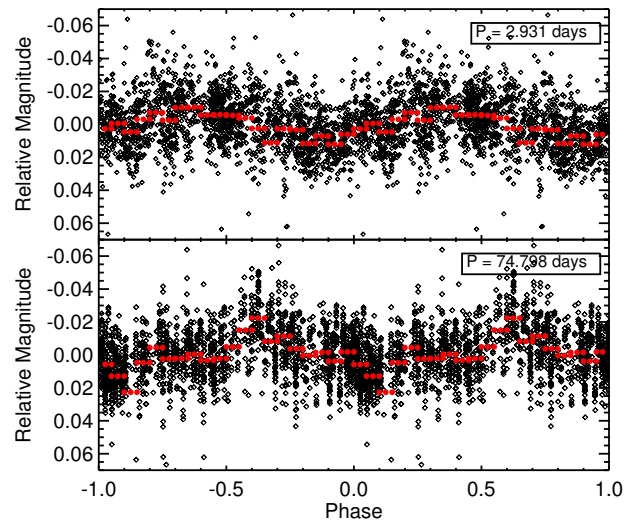


Figure 14. The KELT photometric observations of GW Ori, with the three eclipses removed, phased to the 2.931 (Top) and 74.798 (Bottom) day periods recovered from our LS analysis. Remove 75 day period?

Any theory that seeks to explain these inner eclipses must account for the several pieces of evidence in addition to the updated orbital configuration. Namely, the eclipses span 10 - 50 days in duration, are of variable depth between 0.1 and 0.7 magnitudes, are not strictly periodic with the inner period, and seem to occur at all phases of the outer orbital period. Moreover, our spectra (unwittingly) taken during times of eclipse show no obvious changes in spectral features beyond the normal variability described by Fang et al. (2014). For the epochs where multiple bands existed (e.g., the four eclipses in the Maidanak dataset, which also includes B, R, and noisy U measurements) the eclipse duration was similar in all bands. The star appears slightly redder during eclipse with approximate color changes of $\Delta(B-V)$ and $\Delta(V-R) \sim 0.1$ mag, suggesting dust obscuration. We speculate that these quasi-periodic eclipses may be due to the presence of an unstable circumbinary disk around

A and B or possibly the result of eclipses of the A star by accretion streams onto either the circumstellar disk of A or B.

Lastly, we searched for periodicity in the lightcurve beyond the inner and outer orbital periods. After removing obvious eclipse events, we used the Lomb-Scargle (LS) periodicity search algorithm (Lomb 1976; Scargle 1982) (within the VARTOOLS analysis package; Hartman & Bakos 2016) to search for periodic variability from 1.1 to 100 days in the high cadenced KELT observations. The most significant period we recover is 2.93 days, shown in Figure 14. We suggest that this corresponds to the rotation period of the primary; although we note that Bouvier (1990) and Fang et al. (2014) have derived alternate rotation periods of 3.3 days and 5.0-6.7 days, respectively. Future high precision, high cadence observations of GW Ori will help to unambiguously identify the rotation period of A and possibly B.

4. DISCUSSION

With the newly derived component masses now established, we turn to discussion of the photospheric properties of the stars and the age of the GW Ori system. With these in place, we discuss the system architecture in context of other multiple systems.

4.1. The Age and Photospheric Properties of the GW Ori Stars

We use the spectroscopic constraints on the primary and secondary effective temperatures ($T_{\text{eff}} = 5700 \pm 200 \text{ K}$, $T_{\text{eff}} = 4800 \pm 200 \text{ K}$, respectively) and the collection of multi-band photometry in the literature {fill in information from Keivan} to infer component luminosities for the A and B stars. We note that these values are different from those inferred by Fang et al. (2014), who fit the GW Ori SED assuming that the contribution from the secondary light was negligible. We use the NextGen atmospheres (Hauschildt et al. 1999) and XX reddening laws to infer luminosities of XX and XX for each source. Due to the lingering uncertainties in the orbital parameters, and thus loose constraints on the individual component masses, rather than evaluating the consistency of the pre-Main Sequence model predictions compared to these measured photospheric properties, instead we simply use the pre-Main Sequence models to guide discussion about the individual component properties and system age. In Figure 15 we place these stars on the HR diagram along with representative stellar evolutionary tracks from the MIST models (Choi et al. 2016). The mass tracks start at $0.5 M_{\odot}$ and increase in increments of $0.5 M_{\odot}$; the isochrones are at ages of 0.1, 0.5, 1.0, 2.0, and 3.0 Myr. The positions of A and B in this

diagram are {in}consistent with their measured dynamical masses and indicate ages of 0.5 - 1.5 Myr. Our revised mass for GW Ori A is significantly lower than those estimated by Berger et al. (2011); Fang et al. (2014), and, combined with revising the photospheric properties based upon estimated two components, means that the inferred photospheric properties are now more consistent with a slightly older system than would otherwise be implied ($< 0.5 \text{ Myr}$ if $M_A \geq 3.9 M_{\odot}$). Even with its lower revised mass and luminosity, however, it is likely still true that GW Ori A is a Herbig Ae/Be precursor (as noted by Fang et al. 2014).

In Figure 16, we utilize three MIST models nearest the best-fit masses for each of the stellar components to compute the evolution of the effective temperatures and the V and H -band flux ratios and compare these quantities to the existing photospheric measurements. Beyond the primary and secondary effective temperatures and V -band flux ratio reported in this work, there are two H -band flux ratio constraints from Berger et al. (2011), $f_B/f_A = 0.57 \pm 0.05$ and $f_C/f_A = 0.23 \pm 0.01$ (computed as the weighted mean of all three epochs). In general, the measured effective temperatures and V -band flux ratio agree well with the predictions from the models in the age range 1.0 - 1.7 Myr. The predicted H -band flux ratios are slightly low relative to the Berger et al. (2011) measurements, although still within 20% of the measured value. The predicted V -band flux contribution for the C component is very small ($\lesssim 10\%$), explaining why we were unable to find optical spectroscopic signatures of this component even though it is nearly a solar mass.

As noted by Berger et al. (2011), it is possible that one, two, or all three of the stars might show excess H -band emission due to the presence of a circumstellar disk, and/or accretion signatures above the photospheric emission of these stars. While we find that the measured photospheric properties are reasonably consistent without invoking such an excess, there is circumstantial evidence for the idea beyond the eclipses. (Najita et al. 2003) find blended CO fundamental emission peaks, which Bast et al. (2011) suggest might actually be the blended profiles of emission originating from physically distinct regions, e.g., individual circumstellar disks around the A and B stars. It may also be possible that the CO fundamental emission is consistent with with radius at the inner edge of the circumtriple disk, cleared by the $\sim 9 \text{ au}$ orbit of the C component.

4.2. The GW Ori Triple System in Context

The many unique datasets presented in this paper have enabled us to paint a detailed picture of the

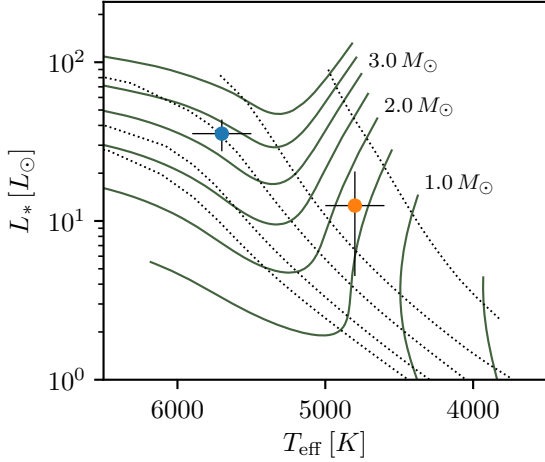


Figure 15. GW Ori A and B placed on the pre-Main Sequence HR diagram. Mass tracks are in increments of $0.5 M_{\odot}$ from $0.5 M_{\odot}$ to $4.0 M_{\odot}$, and isochrones label 0.1, 0.5, 1, 2, 3 Myr ages.

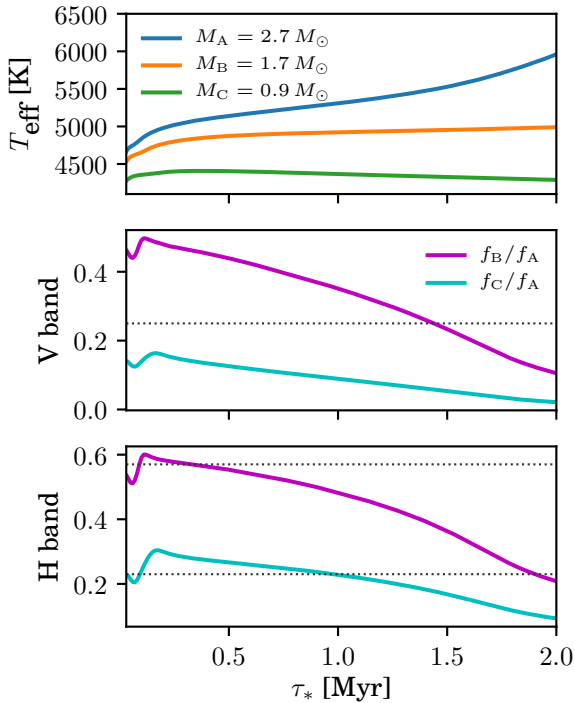


Figure 16. Relative photospheric properties of the GW Ori stellar components as a function of age, using the MIST pre-Main Sequence evolutionary models and assuming the stars are coeval. The measured effective temperatures for the primary and secondary ($T_{\text{eff}} = 5700 \pm 200$ K and $T_{\text{eff}} = 4800 \pm 200$ K, respectively), the V -band flux ratio ($f_B/f_A = 0.25 \pm 0.05$), and the H -band flux ratios ($f_B/f_A = 0.57 \pm 0.05$ and $f_C/f_A = 0.23 \pm 0.01$; Berger et al. 2011) are all roughly consistent with the model predictions for ages of 0.7 - 1.5 Myr.

GW Ori system. It is young (0.7 - 1.5 Myr), contains

a considerable amount of stellar mass ($M_{\text{tot}} = 5.29 \pm 0.09 M_{\odot}$), and hosts a massive disk ($M_{\text{disk}} \approx 0.1 M_{\odot}$), which makes it an extremely interesting system to study in the context of theories about star and planet formation, migration, and stability. In this final section, we aim to place GW Ori into this broader context with other pre-Main Sequence multiple and hierarchical triple systems.

We estimated the total disk mass of GW Ori using the results from our ^{13}CO and C^{18}O modeling in §3.1, which we emphasize are actually indirect measurements that rely upon an uncertain conversion factor between CO and H_2 (and to a lesser degree, the gas to dust ratio). We find slightly larger disk masses when modeling C^{18}O compared to ^{13}CO , which is in conflict with the finding of Fang et al. (2017) that C^{18}O must be depleted relative to ^{13}CO . We attribute the differences in our disk masses to insufficiently complex models of disk structure and note that in general estimating disk masses from CO is notoriously difficult (Yu et al. 2017). In the context of the large disk mass survey by Andrews et al. (2013), GW Ori’s disk mass is slightly larger than the mean predicted value for its stellar mass, although still consistent with the large 1σ envelope in this relationship at high stellar masses. In light of this large disk mass, we investigate whether the disk is Toomre stable today. We use the more massive M_{disk} values from the C^{18}O results to derive a lower bound on Toomre’s Q parameter

$$Q = \frac{c_s \Omega}{\pi G \Sigma} = \sqrt{\frac{k_B M_{\text{tot}}}{\pi^2 \mu m_H G}} \sqrt{\frac{T(r)}{r^2 \Sigma^2(r)}}. \quad (2)$$

For the range of disk parameters determined from our CO fitting, the minimum value is $Q \approx 100$, which occurs far in the outer disk at $r \sim 300$ au—the disk is not currently undergoing disk instability ($Q \approx 1$).

Now we turn to a brief discussion of a few relevant analogues to the GW Ori system. There are now at least four circumbinary disks around short period (10 - 20 days) eccentric binaries across a range of stellar masses which all show alignment between the stellar orbital plane and the circumbinary disk to within 3 deg: UZ Tau E, V4046 Sgr, AK Sco, and DQ Tau (Jensen et al. 2007; Rosenfeld et al. 2012; Czekala et al. 2015b, 2016). These findings agree well with the low mutual inclinations found for *Kepler* circumbinary planets (Winn & Fabrycky 2015), and if statistically significant, have exciting implications for a large circumbinary planet occurrence rate (Li et al. 2016). Of course, severe selection effects are at work in both samples, and so care must be taken when extrapolating these results to the population at large. Within this context, GW Ori stands apart due to the fact that its stellar orbit is *not* aligned with

the disk. This may be a consequence of the larger stellar masses involved, the longer orbital period(s), and/or the presence of a tertiary. Here we examine several other longer period systems which show significantly non-zero mutual inclinations, and show that the large mutual inclinations found in GW Ori are not as unique when considering other longer period systems.

KH 15D is an eccentric ($e = 0.6$) binary system with a slightly longer period than the aforementioned systems (48 days), and hosts a circumbinary dust ring misaligned by 10 - 20 deg from the stellar orbit (Chiang & Murray-Clay 2004; Capelo et al. 2012). The eccentric stellar orbit and disk misalignment causes dramatic photometric eclipse events as stars are screened by the edge of the dust disk. The eclipses also come and go as the ring precesses about the binary. The edge of the occulting disk must be necessarily sharp, which leads to the idea that the ring is confined to a narrow region by a planet at 4 au. The disk and stellar orbital misalignment may be driven by dynamical interactions between the eccentric binary and the disk (e.g., Martin & Lubow 2017; Zanazzi & Lai 2017).

Moving to still larger orbital separations, the frequency of disk-stellar orbital alignment becomes less clear, mainly due to incomplete orbital coverage due to longer periods. Consider GG Tau A, which is a triple system with circumstellar disks around each of three components as well as a larger circumtriple disk. The circumtriple disk is comprised of a dense ring containing 80% of the mass and an outer gas disk extending up to 800 au and is of similar mass to that of the GW Ori disk ($0.12 M_{\odot}$; Guilloteau et al. 1999). The stellar architecture of GG Tau A is rather different than GW Ori, however. The primary star Aa is $0.78 M_{\odot}$, which is in an “outer” orbit with another binary, Ab1 - Ab2, which together have a combined mass of less than $0.7 M_{\odot}$ (Dutrey et al. 2016). The orbital elements of the triple system still have some uncertainty, but Nelson & Marzari (2016) make a convincing dynamical argument that the outer orbit has a semi-major axis of 62 au and is likely coplanar with the outer circumtriple ring. Further astrometric observations are required to definitively confirm this low mutual inclination.

Recently, the massive transition disk system HD 142527 ($M_* = 2.0 M_{\odot}$, $M_{\text{disk}} \sim 0.1 M_{\odot}$) was discovered to have a M dwarf companion orbiting inside its large disk cavity (Biller et al. 2012; Lacour et al. 2016). The presence of this companion provides a possible explanation for why a smaller, inner disk in this system appears to be highly misaligned (~ 70 deg Avenhaus et al. 2014; Marino et al. 2015), which may be driven by secular precession resonance between the disk and the companion (Owen &

Lai 2017). The extreme mass ratio between the M dwarf and the primary ($q = 0.05 - 0.10$) puts the HD 142527 system in a different class of multiple star systems than those we have considered so far. Even though the system parameters do not map directly to sources like GW Ori, these dynamical effects are still important to consider, especially since most existing observations do not have sufficient sensitivity to detect such small companions for most sources (GW Ori included).

At younger ages, the Class 1 binary system L1551 IRS 5 is an interesting analogue because it hosts a large circumbinary disk ($r \sim 500$ au, $M_{\text{disk}} \approx 0.07 M_{\odot}$; Eisner 2012; Takakuwa et al. 2017) outside of two circumstellar disks. The binary is on a wide orbit ($a = 70$ au), to which the circumstellar disks are misaligned by up to 25 degrees. The circumstellar disks are probably aligned with the rotation of the outer circumbinary envelope, which may indicate that the stars were formed by rotationally-driven fragmentation, preserving this orientation (Lim et al. 2016). Surprisingly, Keplerian models of the central stellar mass suggest that only $0.8 M_{\odot}$ is required to explain the rotational velocity of the circumbinary disk, so the particulars of this system also differ from GW Ori in meaningful ways. Another binary system with misaligned protoplanetary disks (though no circumbinary disk) is HK Tau (Jensen & Akeson 2014). Although the stellar orbit is wide (~ 386 au separation) and not yet well defined, the current geometry indicates that at least one and possibly both protoplanetary disks are misaligned with the stellar orbit, likely as a result of their formation rather than any subsequent dynamical evolution.

The most recent example of a misaligned circumbinary disk is in the TWA 3A system (Kellogg et al. 2017), which hosts a circumbinary disk within a hierarchical triple system of stars of near equal mass (SpTs M3 - M4). The “inner” binary Aa-Ab has a 35 day eccentric $e = 0.63$ orbit and hosts a small disk extending 25 au in size (Andrews et al. 2010), while the “outer” orbit A-B takes 200-800 years, and its orbital parameters are not yet fully known. Although the absolute inclinations are not yet known, the parameter space is sufficiently constrained such that it is likely that all three planes (the inner orbit, outer orbit, and circumbinary disk) are misaligned by at least 30 degrees. The Aa-Ab circumbinary disk mutual inclination may be attributable to torques on the disk incurred by the distant B companion.

Of all these T Tauri sources surveyed, GW Ori remains the largest in terms of stellar mass. The configuration of GW Ori proved relatively difficult to probe via traditional detection techniques, requiring sustained, long-term radial velocity monitoring over 35 years, as well as

sophisticated care and attention to derive a radial velocity solution for such a blended source. Finally, resolved submm interferometric observations were necessary to measure the inclination of the circumtriple disk. Looking forward, sustained campaigns of astrometric monitoring will be most helpful for definitively constraining the orbital inclinations.

Although there may still be significant dynamical evolution in the architecture of the GW Ori system before it reaches the Main Sequence, it is worth briefly considering how its orbital parameters compare to the general population of triple stars, even though this population of older systems may have experienced significant dynamical evolution. Among late B star primaries (which GW Ori A will be on the Main Sequence), 13% of systems have multiplicity of three or higher (Eggleton & Tokovinin 2008); this fraction is roughly constant across spectral types B–G. In a detailed analysis of higher-order multiple systems, Tokovinin (1997) found that the ratio $P_{\text{long}}/P_{\text{short}}$ was greater than 10 in almost all systems, presumably reflecting which orbits are stable. While GW Ori's ratio (17) is smaller than in many hierarchical systems, it is not an outlier among triple systems. Tokovinin (1997, 2017) find that the distribution of mutual inclinations of the orbits in triple systems is inconsistent both with complete alignment of the inner and outer orbits (zero mutual inclination) as well as completely independent inclinations (randomly distributed). For triples with outer projected separation < 50 au the average misalignment is 20 degrees, while orbits wider than 1000 au are not preferentially aligned. The population of misaligned triples may be the result of accretion of gas with randomly aligned angular momentum at the epoch of star formation.

Like most multiple stars, the GW Ori system likely formed through turbulent fragmentation, possibly at larger separations than they are now, and then hardened through decay via dynamical interactions, accretion, and the interaction of the circumstellar disks (Offner et al. 2010; Bate 2012). Continued study of the GW Ori system, including spatially resolving the innermost regions to discover circumstellar disks and their relative inclinations, will be valuable to further understanding its formation process.

5. SUMMARY AND CONCLUSIONS

In this work we:

- Used spatially and spectrally resolved ALMA observations of the GW Ori circumtriple disk to derive a dynamical mass for GW Ori of $M_{\text{tot}} = 5.29 \pm 0.09 M_{\odot}$. We find the disk is large ($r_{\text{CO}} \sim$

1300 au), massive ($M_{\text{disk}} \sim 0.1 M_{\odot}$), and has an inclination of $i_{\text{disk}} = 137.6 \pm 2.0$ deg.

- Used 35 years of high resolution optical spectra to derive new double-lined spectroscopic radial velocities, to which we then fit a hierarchical triple orbit, finding a 241 day inner period (A-B) and a 11.5 year outer period (AB - C). When we combine the radial velocity constraints with the disk based constraint on M_{tot} , we find stellar masses of $M_A=2.7 M_{\odot}$, $M_B=1.7 M_{\odot}$, $M_C=0.9 M_{\odot}$, to a precision of $\pm 0.3 M_{\odot}$.
- Combined the radial velocity data with the astrometric data from Berger et al. (2011) to perform a joint RV-astrometric fit and find large mutual inclinations between the stellar orbits and the disk ($\Phi_{\text{in}} = 44 \pm 5$ deg, $\Phi_{\text{out}} = 54 \pm 7$ deg).
- Placed GW Ori A and B on the HR diagram, and find that their stellar properties are broadly consistent with the predictions of pre-Main Sequence models for their measured masses at an age of ≈ 1 Myr.
- Published a lightcurve with a 30 year baseline and identified several new eclipse events. We also identified a 0.2 mag amplitude mode of variability phased with the outer orbital period, suggesting that at apoastron the A-B binary may be partially obscured by micron-sized grains in the circumtriple disk cavity.
- Placed GW Ori in the context of other pre-Main Sequence multiple systems. While short period eccentric binary systems generally seem to have low mutual inclinations with their circumbinary disks, there are a number of longer period systems that exhibit significant mutual inclinations.

Given its uniquely large stellar mass, massive circumtriple disk, and puzzling eclipse behavior, GW Ori should remain a high priority target to study a unique class of dynamical interactions in pre-Main Sequence multiple systems.

IC acknowledges support from the Smithsonian Institution and Stanford KIPAC for the production of this manuscript. IC acknowledges helpful conversations with Maxwell Moe about GW Ori and related systems; and would like to thank Eric Nielsen, Bruce Macintosh, and Rebekah Dawson for helpful discussions about astrometry and orbital dynamics. SA acknowledges the very helpful support provided by the NRAO Student Observing Support program related to the early development

of this project. This paper makes use of the following ALMA data: [XX](#). ALMA is a partnership of ESO (representing its member states), NSF (USA), and NINS (Japan), together with NRC (Canada) and NSC and ASIAA (Taiwan), in cooperation with the Republic of

Chile. The Joint ALMA Observatory is operated by ESO, AUI/NRAO, and NAOJ. This research made extensive use of the Julia programming language ([Bezanson et al. 2017](#)) and Astropy ([Astropy Collaboration et al. 2013](#)).

REFERENCES

- Andrews, S. M., Czekala, I., Wilner, D. J., et al. 2010, [ApJ](#), **710**, 462
- Andrews, S. M., Rosenfeld, K. A., Kraus, A. L., & Wilner, D. J. 2013, [ApJ](#), **771**, 129
- Astropy Collaboration, Robitaille, T. P., Tollerud, E. J., et al. 2013, [A&A](#), **558**, A33
- Avenhaus, H., Quanz, S. P., Schmid, H. M., et al. 2014, [ApJ](#), **781**, 87
- Bast, J. E., Brown, J. M., Herczeg, G. J., van Dishoeck, E. F., & Pontoppidan, K. M. 2011, [A&A](#), **527**, A119
- Bate, M. R. 2012, [MNRAS](#), **419**, 3115
- Berger, J.-P., Monnier, J. D., Millan-Gabet, R., et al. 2011, [A&A](#), **529**, L1
- Bezanson, J., Edelman, A., Karpinski, S., & Shah, V. B. 2017, SIAM Review, **59**, 65
- Biller, B., Lacour, S., Juhász, A., et al. 2012, [ApJL](#), **753**, L38
- Bouvier, J. 1990, [AJ](#), **99**, 946
- Brown, T. M., Baliber, N., Bianco, F. B., et al. 2013, [PASP](#), **125**, 1031
- Buchhave, L. A., Bakos, G. Á., Hartman, J. D., et al. 2010, [ApJ](#), **720**, 1118
- Capelo, H. L., Herbst, W., Leggett, S. K., Hamilton, C. M., & Johnson, J. A. 2012, [ApJL](#), **757**, L18
- Chiang, E. I., & Murray-Clay, R. A. 2004, [ApJ](#), **607**, 913
- Choi, J., Dotter, A., Conroy, C., et al. 2016, [ApJ](#), **823**, 102
- Czekala, I., Andrews, S. M., Jensen, E. L. N., et al. 2015a, [ApJ](#), **806**, 154
- Czekala, I., Andrews, S. M., Mandel, K. S., Hogg, D. W., & Green, G. M. 2015b, [ApJ](#), **812**, 128
- Czekala, I., Andrews, S. M., Torres, G., et al. 2016, [ApJ](#), **818**, 156
- Czekala, I., Mandel, K. S., Andrews, S. M., et al. 2017, [ApJ](#), **840**, 49
- Dolan, C. J. 2000, PhD thesis, Department of Astronomy, University of Wisconsin–Madison, 475 North Charter Street, Madison, WI 53706
- Dolan, C. J., & Mathieu, R. D. 2001, [AJ](#), **121**, 2124
- . 2002, [AJ](#), **123**, 387
- Duchêne, G., & Kraus, A. 2013, [ARA&A](#), **51**, 269
- Dullemond, C. P. 2012, RADMC-3D: A multi-purpose radiative transfer tool, [Astrophysics Source Code Library](#), [ascl:1202.015](#)
- Dutrey, A., Di Folco, E., Beck, T., & Guilloteau, S. 2016, [A&A Rv](#), **24**, 5
- Eggleton, P. P., & Tokovinin, A. A. 2008, [MNRAS](#), **389**, 869
- Eisner, J. A. 2012, [ApJ](#), **755**, 23
- Fang, M., Sicilia-Aguilar, A., Roccatagliata, V., et al. 2014, [A&A](#), **570**, A118
- Fang, M., Sicilia-Aguilar, A., Wilner, D., et al. 2017, [A&A](#), **603**, A132
- Fekel, Jr., F. C. 1981, [ApJ](#), **246**, 879
- Foreman-Mackey, D., Hogg, D. W., Lang, D., & Goodman, J. 2013, [PASP](#), **125**, 306
- Fürész, G. 2008, Ph.D. Thesis, Univ. Szeged, Hungary
- Gelman, A., Carlin, J. B., Stern, H. S., et al. 2014, Bayesian data analysis, Vol. 2 (CRC press Boca Raton, FL)
- Goodman, J., & Weare, J. 2010, Communications in Applied Mathematics and Computational Science, **5**, 65
- Guilloteau, S., Dutrey, A., & Simon, M. 1999, [A&A](#), **348**, 570
- Hartman, J. D., & Bakos, G. Á. 2016, [Astronomy and Computing](#), **17**, 1
- Hartmann, L., Calvet, N., Gullbring, E., & D'Alessio, P. 1998, [ApJ](#), **495**, 385
- Hauschildt, P. H., Allard, F., Ferguson, J., Baron, E., & Alexander, D. R. 1999, [ApJ](#), **525**, 871
- Henkel, C., Wilson, T. L., Langer, N., Chin, Y.-N., & Mauersberger, R. 1994, in Lecture Notes in Physics, Berlin Springer Verlag, Vol. 439, The Structure and Content of Molecular Clouds, ed. T. L. Wilson & K. J. Johnston, 72
- Husser, T.-O., Wende-von Berg, S., Dreizler, S., et al. 2013, [A&A](#), **553**, A6
- Jensen, E. L. N., & Akeson, R. 2014, [Nature](#), **511**, 567
- Jensen, E. L. N., Dhital, S., Stassun, K. G., et al. 2007, [AJ](#), **134**, 241
- Jonkheid, B., Faas, F. G. A., van Zadelhoff, G.-J., & van Dishoeck, E. F. 2004, [A&A](#), **428**, 511
- Kamp, I., & Dullemond, C. P. 2004, [ApJ](#), **615**, 991
- Kellogg, K., Prato, L., Torres, G., et al. 2017, [ApJ](#), **844**, 168

- Kounkel, M., Hartmann, L., Loinard, L., et al. 2017, *ApJ*, 834, 142
- Kuhn, R. B., Rodriguez, J. E., Collins, K. A., et al. 2016, *MNRAS*, 459, 4281
- Kurtz, M. J., & Mink, D. J. 1998, *PASP*, 110, 934
- Lacour, S., Biller, B., Cheetham, A., et al. 2016, *A&A*, 590, A90
- Latham, D. W. 1992, in Astronomical Society of the Pacific Conference Series, Vol. 32, IAU Colloq. 135: Complementary Approaches to Double and Multiple Star Research, ed. H. A. McAlister & W. I. Hartkopf, 110
- Li, G., Holman, M. J., & Tao, M. 2016, *ApJ*, 831, 96
- Lim, J., Yeung, P. K. H., Hanawa, T., et al. 2016, *ApJ*, 826, 153
- Lomb, N. R. 1976, *Ap&SS*, 39, 447
- Lynden-Bell, D., & Pringle, J. E. 1974, *MNRAS*, 168, 603
- Marino, S., Perez, S., & Casassus, S. 2015, *ApJL*, 798, L44
- Martin, R. G., & Lubow, S. H. 2017, *ApJL*, 835, L28
- Mathieu, R. D., Adams, F. C., Fuller, G. A., et al. 1995, *AJ*, 109, 2655
- Mathieu, R. D., Adams, F. C., & Latham, D. W. 1991, *AJ*, 101, 2184
- Murray, C. D., & Correia, A. C. M. 2010, Keplerian Orbits and Dynamics of Exoplanets, ed. S. Seager, 15
- Najita, J., Carr, J. S., & Mathieu, R. D. 2003, *ApJ*, 589, 931
- Nelson, A. F., & Marzari, F. 2016, *ApJ*, 827, 93
- Offner, S. S. R., Kratter, K. M., Matzner, C. D., Krumholz, M. R., & Klein, R. I. 2010, *ApJ*, 725, 1485
- Owen, J. E., & Lai, D. 2017, *MNRAS*, 469, 2834
- Prantzos, N., Aubert, O., & Audouze, J. 1996, *A&A*, 309, 760
- Rosenfeld, K. A., Andrews, S. M., Hughes, A. M., Wilner, D. J., & Qi, C. 2013, *ApJ*, 774, 16
- Rosenfeld, K. A., Andrews, S. M., Wilner, D. J., & Stempels, H. C. 2012, *ApJ*, 759, 119
- Scargle, J. D. 1982, *ApJ*, 263, 835
- Shappee, B. J., Prieto, J. L., Grupe, D., et al. 2014, *ApJ*, 788, 48
- Shevchenko, V. S., Grankin, K. N., Ibragimov, M. A., & Melnikov, S. Y. 1992, Information Bulletin on Variable Stars, 3746
- Shevchenko, V. S., Grankin, K. N., Mel'Nikov, S. Y., & Lamzin, S. A. 1998, *Astronomy Letters*, 24, 528
- Siverd, R. J., Beatty, T. G., Pepper, J., et al. 2012, *ApJ*, 761, 123
- Takakuwa, S., Saigo, K., Matsumoto, T., et al. 2017, *ApJ*, 837, 86
- Tokovinin, A. 2017, *ApJ*, 844, 103
- Tokovinin, A. A. 1997, *A&AS*, 124
- Torres, G., Neuhäuser, R., & Guenther, E. W. 2002, *AJ*, 123, 1701
- Winn, J. N., & Fabrycky, D. C. 2015, *ARA&A*, 53, 409
- Yu, M., Evans, II, N. J., Dodson-Robinson, S. E., Willacy, K., & Turner, N. J. 2017, *ApJ*, 841, 39
- Zanazzi, J. J., & Lai, D. 2017, ArXiv e-prints, arXiv:1706.07823 [astro-ph.EP]